

Confinement and Transport Research in Alcator C-Mod

M. Greenwald, N. Basse, P. Bonoli, R. Bravenec¹, E. Edlund, D. Ernst, C. Fiore, R. Granetz, A. Hubbard, J. Hughes, I. Hutchinson, J. Irby, B. LaBombard, L. Lin, Y. Lin, B. Lipschultz, E. Marmor, D. Mikkelsen², D. Mossessian, P. Phillips¹, M. Porkolab, J. Rice, W. Rowan¹, S. Scott², J. Snipes, J. Terry, S. Wolfe, S. Wukitch, K. Zhurovich - *Plasma Science & Fusion Center, Massachusetts Institute of Technology, Cambridge, MA, USA*

1 University of Texas, Austin, TX, USA

2 Princeton Plasma Physics Laboratory, Princeton, NJ, USA

contact information for main author:

Martin Greenwald
MIT - Plasma Science & Fusion Center
175 Albany St.
Cambridge, MA 02138
USA
e-mail: g@psfc.mit.edu
phone: (617) 253-6053, 253-5391
fax: (617) 253-0627

Confinement and Transport Research in Alcator C-Mod

M. Greenwald, N. Basse, P. Bonoli, R. Bravenec¹, E. Edlund, D. Ernst, C. Fiore, R. Granetz, A. Hubbard, J. Hughes, I. Hutchinson, J. Irby, B. LaBombard, L. Lin, Y. Lin, B. Lipschultz, E. Marmor, D. Mikkelsen², D. Mossessian, P. Phillips¹, M. Porkolab, J. Rice, W. Rowan¹, S. Scott², J. Snipes, J. Terry, S. Wolfe, S. Wukitch, K. Zhurovich - Plasma Science & Fusion Center, Massachusetts Institute of Technology, Cambridge, MA, USA

¹ University of Texas, Austin, TX, USA

² Princeton Plasma Physics Laboratory, Princeton, NJ, USA

e-mail contact of main author: g@psfc.mit.edu

Abstract

Global and local transport experiments in Ohmic, L-mode and H-mode regimes on the Alcator C-Mod tokamak are summarized. For Ohmic plasmas, earlier results derived for energy confinement scaling in the Alcator (linear) regime have been confirmed and the saturated confinement regime has been shown to be equivalent to L-mode. For auxiliary heated regimes, C-Mod provided a unique laboratory to test the standard scaling laws which had been previously derived. C-Mod's L-mode performance matches the L-mode scaling laws quite well, but the confinement times in H-mode were about 50% above the existing H-mode scaling laws. This difference was significant and pointed up shortcomings in the range and conditioning of the existing database. H-mode studies emphasize quasi-steady regimes with good energy confinement, no impurity accumulation and no large ELMs. A new H-mode regime, where the pedestal is regulated by a continuous quasi-coherent mode has been investigated extensively. The regime is most accessible at higher safety factor, triangularity, collisionality and at low ion mass, suggesting that the mode is a form of resistive ballooning. Studies on C-Mod first showed the quantitative link between edge temperatures, core temperature gradients and core confinement. This link unified L-mode and H-mode and established a strong connection between local and global transport. Further work on the role of critical gradient lengths and marginal stability lent quantitative support to the ITG theories for ion transport and have helped elucidate nonlinear saturation mechanisms for the turbulence. Local transport studies demonstrated connections between transport channels, with energy, particle and momentum transport varying across regimes in similar ways. Experiments carried out in collaboration with the DIII-D, ASDEX-U and JET groups confirmed the dimensionless scaling approach over the widest available range in machine sizes. These studies suggest that plasma physics is the dominant influence on transport in the core *and* pedestal for standard L- and H-mode discharges. Dimensionless scaling experiments have shown a strong improvement in confinement with the normalized gyro-size ($1/\rho^*$). Confinement was found to be Bohm-like in L-mode and gyro-Bohm-like in H-mode. These experiments also showed a strong degradation in confinement with collisionality. Other articles in this issue discuss impurity transport, momentum transport, H-mode pedestal and threshold physics and internal transport barrier regimes.

1. Introduction

Alcator C-Mod is a compact high-field diverted tokamak with molybdenum plasma facing components and strong ICRF heating. It has a nominal major radius, $R = 0.66$ m and minor radius, $a = 0.22$ m. For transport studies, parameter ranges span; $I_p = 0.24 \rightarrow 2$ MA; $B_T = 2.0 \rightarrow 8.0$ T; $P_{\text{INPUT}} = 0.25 \rightarrow 5$ MW; $n_e = 0.24 \rightarrow 6 \times 10^{20}/\text{m}^3$; $\kappa = 0.94 \rightarrow 1.85$; $\delta = 0.0 \rightarrow 0.85$; $a = 0.17 \rightarrow 0.24$. The principal heating scenario employed is first harmonic hydrogen in a deuterium majority plasma at 5.3 T and an ICRF frequency near 80 MHz. The same frequency is used for heating a He3 minority at 7.9 T. Half of the RF power is available from sources tunable from 50 – 80 MHz, expanding the range of toroidal fields which can be efficiently heated. Second harmonic deuterium majority and mode conversion heating scenarios have also been exploited. Details of the ICRF systems and results can be found in reference [1].

C-Mod operation has several unique features with respect to transport studies. Because the B/R ratio is high, the machine typically runs at densities which are 10 times higher than conventional tokamaks. This extends operation to higher collisionality, lower fast-ion content and leads to the reactor relevant condition of equilibrated electrons and ions in most regimes. The exclusive use of RF and Ohmic heating allows the study of transport in discharges with no core particle or momentum source. While C-Mod operates in a unique dimensional parameter range it can be run as to overlap in dimensionless parameters with larger low-field tokamaks. This combination allows us to 1) dramatically extend the range of engineering parameters in global scaling studies; 2) perform dedicated dimensionless identity experiments where all dimensionless parameters are held fixed between two or more machines; 3) perform

dimensionless scaling experiments, where one dimensionless parameter is scanned over a wide range between two or more machines with other dimensionless parameters held fixed; and 4) extend physics studies to unique regions of dimensionless parameter space. C-Mod has a strong diagnostic set for transport studies which is described in detail in reference [2].

Alcator C-Mod addresses a broad range of transport issues emphasizing those areas where it has unique capabilities, is in unique parameter regimes, observes unique or unusual phenomena, or can make important comparisons with other devices. Comparisons with theory and modeling form an important part of the program with theory playing a critical role in motivating experiments and in determining their design. This article will cover only global and local transport studies in Ohmic, L-mode and H-mode plasmas, with emphasis on the latter. Work on the H-mode has included studies of local threshold conditions and comparisons with theory; demonstration of regimes with good confinement but no large, potentially destructive ELMs; links between core and edge confinement and connections to theoretical models of marginal stability and dimensionless scaling of the core and pedestal plasma profiles. Other articles in this issue discuss impurity transport [3], momentum transport [4], H-mode pedestal and threshold physics [5] and internal transport barrier regimes [6].

2. Confinement in Ohmically Heated Plasmas

Ohmic plasmas have been studied over a wide range in plasma current ($I_p = 0.24 \rightarrow 2.0$ MA), toroidal field ($B_T = 2.0 \rightarrow 8.0$ T), plasma density ($n_e = 0.24 \rightarrow 6 \times 10^{20}/\text{m}^3$), plasma shape

($\kappa = 0.94 \rightarrow 1.85$) and size ($a = 0.17 \rightarrow 0.24$). While the heating power is only applied in the electron channel, for all but the lowest density C-Mod discharges, the electron-ion heat exchange is fast and significant power flows through the ion channel as well. Ohmic plasmas have a low β (0.1-0.5%), large normalized size, $1/\rho^*$ (200-500) and a wide range of collisionality (.04-4.5). The central electron temperature, $T_e(0)$, in these discharges ranges from 700 to 3500 eV. Confinement properties are studied mostly via analysis and integration of plasma density and temperature profiles. (At the very low β_p which is typical of Ohmic discharges, the MHD analysis of the stored energy can be burdened by significant systematic errors. For discharges with auxiliary heating, where both methods are valid, the agreement is excellent – typically within 10%). Four distinct confinement modes are observed. At very low densities the Alcator or linear Ohmic confinement (LOC) regime is recovered in C-Mod. This regime, which was first discovered on Alcator A [7], has the energy confinement time, τ_E , proportional to plasma density. At all other densities (which encompasses most operations), Ohmic discharges are in the saturated Ohmic confinement regime (SOC) where energy confinement is independent of density. Confinement scaling and transport properties of these discharges are essentially indistinguishable from auxiliary heated L-mode plasmas and may properly be called “Ohmic L-modes” [8]. When the plasma current is raised and/or the toroidal field is lowered such that q_{95} approaches 2.5, Ohmic H-modes are produced. These discharges are similar to auxiliary heated H-modes, but because of the low heating power, they remain close to the L/H threshold and tend to be transient and to have only moderately improved confinement. Ohmic discharges can also develop internal transport barriers (ITB). Most Ohmic H-modes develop this feature spontaneously if the H-mode is sustained for more than a few confinement times [9]. Ohmic ITBs are also produced by pellet injection [10, 11].

2a. Linear Ohmic Regime

The linear Ohmic confinement regime occurs only in a narrow range of densities, very roughly in the range of 10-20% of the density limit. This range is bounded on the lower end by the appearance of runaway electrons or locked modes[12] and by confinement saturation on the upper end. The saturation point can be characterized on C-Mod by $n_{20} \sim 4/q$, where n_{20} is the line averaged plasma density in $m^3/1 \times 10^{20}$ and q is the MHD safety factor. Sufficient data to reliably scale the saturation threshold do not exist however. Figure 1 shows the energy confinement time vs density for a set of data at fixed toroidal field and current. For the standard shape, with $k \sim 1.5$, the break between regimes is observed at approximately $n_e \sim 0.6 \times 10^{20} / m^3$. Regressions using a larger set of data, (with major radius fixed), give

$$\tau_E = 0.156 n_e^{0.95} a^{2.1} q^{1.2}$$

where τ_E is in seconds, n_e is in $10^{20}/m^3$ and a is in m. The fit is shown in figure 2a. The size scale is not reliable because of the narrow range of data, so this result is reasonably close to the so-called neo-Alcator scaling $\tau_E = 0.066 n R^2 a \kappa^{0.5} q$ [7, 13] with which the data are compared in figure 2b. The observed scaling with nq also helps to explain why the neoAlcator regime is more restricted in modern machines. With their stronger shaping, the increase of confinement with density is so rapid in these devices that it quickly reaches the L-mode levels and saturates.

It seems clear from the higher elongation data in figure 1 that the linear and saturated confinement laws do not add in quadrature as early authors had suggested [13]. The sharp transition suggests instead, proximity to marginal stability. Careful transport analysis with the TRANSP code [14] shows that, for these low density plasmas, the loss channel is indeed in the electrons and that the ions are conducting a negligible fraction of the power. The saturation seen at higher densities can be understood as the appearance of ion turbulence which is driven when the ion heat flux becomes difficult to carry via collisional transport [15]. A useful way of looking at the break between regimes is that, as the plasma density and safety factor are lowered, a new electron loss channel opens up, conducts all available power and reduces the ion heat flux allowing it to drop to neoclassical levels. At high densities, peaking the density profiles stabilizes the ion channel (via lowering $\eta_i \equiv L_n/L_T$) and allows the neoAlcator regime to be extended [26].

2b. Saturated Ohmic Regime

As the plasma density is raised the Ohmic power is coupled to the ions and the density dependence of the energy confinement disappears. An unconstrained regression to saturated Ohmic C-Mod data is shown in figure 3a and yields:

$$\tau_E = 0.039 I_p^{0.98} n_e^{0.12} m^{0.24} P_{OH}^{-0.60} \quad [8]$$

The covariance between Ohmic power and current has long been noted limiting the reliability of such scalings. However the resemblance to standard L-mode scaling derived for experiments with strong auxiliary heating is striking. The Ohmic data can also be compared to this scaling law and as shown in figure 3b yield reasonable agreement. The distinction between the saturated Ohmic regime and L-mode is probably not a useful one.

3. L-mode Confinement in Auxiliary Heated Plasmas

Using the ICRF systems described in reference [1], input powers have been raised to 5 MW resulting in ion and electron temperatures as high as 6 keV. The resonant nature of ICRF heating constrains the values of B_T for which efficient heating can be achieved. However by employing various scenarios, (D/H minority, D/He3 minority, 2nd harmonic D majority, He3/D mode conversion) and various RF frequencies (50, 70, 80 MHz), experiments with auxiliary heating have been carried out in C-Mod from 2.8 to 8 T. The range of values for plasma current, density and shaping are similar to those described in section 2. Because of the high densities employed, ion tails produced by minority heating are well coupled to the bulk and seldom account for more than 5 or 10% of the stored energy. Under most conditions, low Z impurities tend to be unimportant and Z_{EFF} is not far above 1 [8]. Assuming an L-mode like scaling for impurity confinement, this is equivalent to $Z_{EFF} \propto \text{energy/particle}$. Fitting the available confinement data yields for L-mode plasmas, including the SOC data, leads to:

$$\tau_E = 0.023 I_p^{0.96} n_e^{-0.10} m^{0.15} B_T^{0.29} \kappa^{0.45} P_{TOT}^{-0.50} [8]$$

Figure 4a shows the results of this regression. Comparison with the ITER89 scaling law [17] is shown in figure 4b.

4. H-Mode

4a. Introduction, L-H transition and Thresholds

Access to H-mode was a critical concern when Alcator C-Mod was under construction, with predictions for the power threshold at the time ranging from 0.1 to 10 MW [18]. When the machine operated, the L/H threshold was found to be in the range 1-2 MW [19]. By extending the range in density and field by significant factors, the C-Mod results helped put the threshold scalings on a much firmer basis [20]. Because of the all-metal first-wall construction and the need to control high Z impurities, good quality, sustained H-modes were not achieved until the machine was boronized [21], however, neutral control via wall conditioning was not an issue in C-Mod. The L/H power threshold was found to scale linearly with nB above a low density limit which was in the range $0.7-0.9 \times 10^{20}$ for typical operating conditions of 5.3T and 0.8-1.0 MA[22]. As discussed above, H-modes could be produced with Ohmic heating alone, at higher currents (to maximize Ohmic power) and at low toroidal field (to minimize the threshold) [23]. Significant hysteresis in the H-mode thresholds was observed, with H/L transitions occurring at less than half the power of forward transitions. Perhaps of greater interest were studies of the threshold based on local edge parameters where transitions when when a critical temperature (or

temperature gradient) was crossed in either direction [24]. The critical temperature was seen to scale with B_T having a value of about 140 eV at 5.3 T [25]. These results are roughly consistent with the transition theories of Guzdar [26]. The total power and critical temperature for the transition was roughly a factor of two higher in discharges where the ion ∇B drift was directed away from a single null x-point compared to discharges with the drift toward the x-point. Recent studies suggest that this can be explained via flows driven in the scrape-off layer by poloidally asymmetric cross-field transport [27]. Details on L/H threshold studies can be found in reference [5]. L/H transitions are rapid in C-Mod, with dramatic drops in edge fluctuations occurring in 50-100 μ secs [21].

4b. H-mode Regimes

H-modes have been studied in C-Mod over a wide range in plasma current (0.4 – 1.2 MA), toroidal field (2.6 – 7.9 T), plasma density ($1.5 - 5.0 \times 10^{20}/\text{m}^3$), plasma shape ($1.55 < \kappa < 1.85$; $0 < \delta < 0.80$) and with RF powers up to 5 MW [21]. In terms of the density limit, H-modes have been studied at $n/n_G = 0.3 - 0.85$. (n_G is the tokamak density limit equal to $I_p/\pi a^2$ [28].) The highest performance H-modes have densities above 4.0×10^{20} and electron and ion temperatures above 4 keV, yielding peak and average pressures of 0.53 MPa and 0.18 MPa respectively. These are perhaps the highest volume averaged plasma pressures ever produced in a magnetic confinement experiment. Pedestal temperatures range from 200-1,000 eV. Density profiles in these H-mode plasmas are quite flat, except in cases where ITBs develop, and Z_{EFF} tends to be

low, ranging from 1.0 to 2.5. An unexpected feature of these torque-free, RF heated discharges is strong co-current rotation, up to 100 km/sec for high performance H-modes [29].

As in other devices, various H-mode regimes are observed in C-Mod, and correspond principally to different edge relaxation mechanisms [30]. When the conducted power is just above the threshold and the edge temperature is low, type III ELMs are seen [31]. These are often regularly spaced, repeating at 1-5 kHz, with each individual ELM having no discernable effect on the core plasma and causing only minimal perturbation to the pedestal. The overall confinement properties of these discharges are poor. At higher pedestal temperatures, the type III ELMs disappear and two types of H-modes can exist. With higher currents and/or with weak shaping, the plasmas tend to be ELM-free. This regime is always transient, with particles and impurities accumulating, leading to a back transition. With stronger shaping or at lower plasma current, high-performance, steady discharges can develop. The discharges are characterized by high levels of recycling light and have been termed Enhanced D_α (EDA) H-modes [32]. While technically free of ELMs, the EDA plasmas are similar in most other respects to type I ELMy discharges commonly found in other devices. However, in the case of EDA, the pedestal is regulated by a continuous quasi-coherent (QC) oscillation in the range of 50-200 kHz [33, 34]. Figure 5 shows the comparison between an ELM-free and an EDA discharge. Most notable is the dramatic drop in radiated power for the EDA case, along with its steady density and stored energy. As the pedestal pressure is raised further (corresponding to the global $\beta_N > 1.2$) small, “grassy” “type II” ELMs appear[34]. These can coexist in EDA discharges as shown in figure 6. At still higher pedestal pressures and at somewhat lower densities, these small ELMs predominate and the QC mode disappears. The type II ELMs can be seen as minor perturbations

in the edge pedestal and SOL particle flux, however, individual ELMs have no discernable effects on global parameters such as stored energy or line-averaged density. They do not correspond to a destruction or severe degradation of the pedestal. As discussed below, unlike the EDA or type III discharges, the pedestal of these plasmas have pressure gradients near or above the ideal stability limit. Type I ELMs, which do transiently destroy the edge pedestal and which can be seen individually on global parameters *have not been seen in C-Mod*. In a very few unusual discharges, large discrete ELMs are observed, but even these do not seem to have the character of type I ELMs. Thus, the “standard” H-modes for C-Mod are EDA or those with type II ELMs. While uncommon on other devices, the EDA regime is apparently not entirely unique to C-Mod. In early JET experiments, a regime dubbed LPC for low particle confinement was observed [35]. This mode has not been produced since, so direct comparisons are not possible, however, in most respects it appears similar to EDA. Dimensionless identity experiments, carried out between C-Mod, ASDEX-upgrade and DIII-D found that in cases where the dimensionless parameters of those machines matched C-Mod EDA plasmas, some signatures of the EDA regimes were observed [36]. JFT-2M has recently reported an HRS (for High-Recycling Steady) H-mode regime, which also shares many of the same characteristics[37]. The HDH (High-Density H-mode) regime seen on the W7AS device also has common features [38]. Further details on the confinement properties of and the boundaries between the H-mode regimes are discussed below. Descriptions of the pedestal profiles and scalings can be found in reference [5].

4c. EDA and Small-ELM H-modes

The EDA and small ELM regimes are of particular importance because they combine good energy confinement, moderate particle and impurity confinement (and thus a potential for steady state operation) without large power or particle impulses to the divertor as is the case for large ELM regimes [34, 39]. Energy confinement in these regimes is typically 80-90% of ELM-free operation [21, 34] (that is, in the early phase of ELM-free operation before impurity accumulation degrades performance.) A general feature of these discharges is an overall increase in the hydrogen Balmer- α light, a decrease in the rate of density rise and lower levels of impurity radiation, all suggesting increased particle transport. Figure 5 compared some important signals from an EDA (with small ELMs) discharge with an ELM-free one. As noted above, the lower level radiated power and steadier confinement of the EDA plasma are significant. The difference in radiation is due to dramatically lower impurity confinement for the EDA case [21]. Impurity transport is discussed in more detail in section 7 and in reference [3]. A summary of features from these regimes is contained in Table I.

Access conditions to the EDA and small ELM regimes have been extensively investigated [34, 40]. Dedicated scans of q (both I_p and B_T), density, power, working gas and shape (elongation, κ and triangularity, δ) were carried out. It was found that EDA and ELMy conditions were more likely at higher safety factor, ($q > 3.5$), higher triangularity, ($\delta > 3.5$) and higher target density. The dependence on triangularity is seen in figure 7a, where a continuous scan from high to low triangularity was carried out for otherwise fixed conditions. The discharge showed a series of sharp transitions between the regimes as the triangularity dropped, spending more and more time in the ELM-free regime and finally becoming purely ELM-free. The

amplitude of the QC mode precisely followed each of these transitions before disappearing. This phenomena has the appearance of “dithering” between the EDA and ELM-free regimes. A closer look reveals substantial structure, with dithering behavior consisting of a series of periodic transitions spaced about 1 msec apart. As seen in fig 7b, a short burst of the QC mode accompanies each EDA period. Similar results were obtained with scans of the safety factor. No obvious dependence of the EDA/ELM-free boundary on κ or input power was found over the ranges studied. EDA discharges produced in Ohmic H-modes (shown in figure 8) show the same accessibility boundaries, thus this regime cannot be attributed to direct effects of RF or of a high-energy minority ion tail [40]. Figure 9 shows the boundary between EDA and ELM-free operation in the q, δ plane. One can see that the boundary is “soft”, that is there is a good deal of overlap between the two sets of data, suggesting additional dependences. It is also interesting to note that very similar plots have been obtained for access to small ELM regimes in other devices [41]. Experiments in majority hydrogen plasmas found EDA operation at lower q values, down to 2.6. As the heating power is increased, the plasma pressure increases and small, type II ELMs begin to dominate[21, 34]. At higher powers, the QC mode disappears entirely and the plasma is regulated by the small ELMs alone. Figure 6 showed traces from several diagnostics depicting these ELMs. Note that the ELMs are “bipolar” on the Balmer- α traces, that is the perturbations are above and below the baseline H_α level. Their MHD characteristics are discussed in reference [42]. Figure 10 shows a boundary between EDA and ELMy discharges in a plot of pedestal temperature vs pressure [43]. It can be seen that EDA tends to be restricted to somewhat lower values of pressures and higher values of collisionality. Results of stability calculations with the ELITE code [44] are also plotted in this figure. Using measured pedestal temperature and density profiles and current profiles computed with comprehensive models for neoclassical

resistivity and bootstrap current, it was found that the EDA/ELM boundary corresponded to the stability boundary for intermediate n coupled peeling/ballooning modes [43].

4d. The QC Mode and EDA

The connection between the appearance of quasi-coherent fluctuations and the EDA H-mode seems to be causal. That is, we find that the QC mode is the probable mechanism by which the pedestal profiles and transport are regulated in an EDA plasma. This conclusion rests on three observations. First, the QC mode is always present in discharges which show the other aspects of the EDA regime – high levels of Balmer- α light (relative to ELM-free H-modes), decreased particle confinement and sharply increased impurity transport relative to ELM-free H-modes. Second, the mode is localized in the steep gradient region of the pedestal. Third, there is a nearly linear relationship observed between the amplitude of the QC mode and the local particle diffusivity at the separatrix. This latter quantity is determined by using local, high-resolution measurements of the density, temperature and Lyman α emission to calculate the ionization source rate across the pedestal and scrape-off layer and dividing by the local electron density gradient to get an effective diffusivity. The result of such calculations is shown in figure 11. A similar dependence has been observed between the mode amplitude, Balmer α level and the pedestal x-ray width [45], the latter quantity being a good measure of local impurity transport.

With the importance of the QC fluctuations established, it is worth describing the mode in somewhat greater detail. It was first observed via reflectometry at 88 GHz [33], with further measurements by electrostatic probes, electromagnetic probes, phase contrast imaging (PCI), gas puff imaging (GPI), beam emission spectroscopy (BES), and heterodyne electron cyclotron emission (HECE) measurements [46, 47]. That is, it can be seen by all diagnostics capable of measuring short wavelength fluctuations in the plasma edge. The fluctuation amplitude is large, with the local $\delta n/n$ reaching 50%. The electromagnetic perturbation is also significant, with $\delta J/(J_{OH}+J_{BS}) \sim 20\%$, the latter number coming from measurements by a pair of magnetic loops mounted on a fast scanning probe and inserted to within 1 cm of the separatrix [46]. While the magnetic perturbation is large, it is usually not observed by the standard set of magnetic probes mounted on the vacuum vessel wall. Typical spectra of the QC mode can be seen in figure 12. The normalized spectral width, $\delta f/f$ is approximately 0.1, though this value may vary from 0.05 to 0.3. Figure 13 shows the evolution of the autopower spectra from PCI measurements vs time. It is customary for the QC mode to sweep down in frequency following the L/H transition. This is believed to result from a change in the Doppler shift that occurs as the H-mode pedestal is established. The mode frequency decreases as the pedestal pressure gradient (and core rotation velocity) increase and the fluctuations have a phase velocity of approximately 1.5 km/sec in the electron diamagnetic direction. The mode has a relatively short wavelength. Figure 14 shows an intensity plot in ω, k space taken from PCI data [48]. Diagnostics capable of measuring the wavelength of the mode cover a range of poloidal locations. These results are summarized in figure 15 where poloidal wavenumbers obtained from PCI, GPI and probes are plotted versus poloidal field angle. The solid line shows the expected result for a field aligned perturbation. The short poloidal wavelength explains why the mode is hard to observe with standard magnetic

pick-up coils. Localization of the mode can be achieved by the BES, GPI, reflectometry and probe data. The mode has a radial extent less than 4 mm, perhaps as small as 1-2 mm and is located just inside the separatrix [49] as seen in figure 16. Similar fluctuations have been seen between ELMs in H-mode discharges on other devices PDX[50], CCT [51], PBX[51] DIII-D[52].

The appearance of coherent modes in a region with pressure gradients near the MHD stability limits and at high collisionality suggests a connection to resistive ballooning. These modes should be destabilized at higher values of $q/m_i^{0.5}$, in qualitative agreement with the EDA threshold studies[53]. While these modes are found to be turbulent if driven far beyond their linear threshold, coherent modes, saturated by quasi-linear flattening of the profiles, have been found in simulations [54]. Three dimensional, electromagnetic fluid codes (DRB [55] and BOUT [56]) have been used to simulate the C-Mod edge plasma. Modes very much like the QC mode were produced and matched the experimental observations in several important ways [48, 55, 57], most notably the mode localization and wavenumber. The three dimensional gyrokinetic code, gs2 [58], also found a strongly growing linear mode in the pedestal. The lack of ELMs in these discharges may be partially explained by the high pedestal collisionality ($\nu^* > 1$). This will tend to suppress the bootstrap current, reducing the drive for current driven modes (peeling) and will destabilize pressure driven modes like resistive ballooning. Even accepting this explanation for the QC mode, several important questions remain. First, it is far from clear what saturates this very large amplitude mode, or what prevents it from spreading in k space and generating broad-band turbulence. Secondly, we do not understand the feedback loop between the mode and the profiles which would be the mechanism by which the pedestal is regulated in the absence

of ELMs leading to an ELM-free steady-state. Finally, we do not understand why the mode is so effective in transporting impurities relative to plasma energy.

4e. H-mode Global Confinement

Energy confinement in C-Mod H-modes provided a test of the global scaling laws developed earlier by international collaborations working on performance projections for ITER [59]. In these studies, a database of ELM-free H-modes was carefully assembled, screened for known adverse effects (eg, high levels of radiated power or MHD fluctuations) and fit to a power law equation. The important fitting parameters included plasma size, density, current, power, toroidal field and elongation, “engineering” variables which can be directly controlled by machine design or operation. C-Mod H-mode data, which became available in 1996, exceeded the ITER93 H-mode confinement predictions, outside the RMS errors of the published regression [21]. The C-Mod data averaged about 2-3 standard deviations above the fit. The likely cause for the failure to predict C-Mod results was the limited parameter range of the data used for the fit compared to the extrapolation to C-Mod parameters and correlations between independent parameters in the database. Following this exercise, data from C-Mod (and additional data from other machines) were included in the international database and the regressions recalculated. The emphasis at this time was on scaling of thermal energy confinement in ELMy discharges, for which C-Mod included EDA and mixed EDA/type II ELMy plasmas. Because of its high plasma density, fast particle content was relatively low for C-Mod, with non-thermal energy typically 5-10% of the total. The results were the ITER97 and

ITER98 H-mode scaling laws which fit the C-Mod data reasonably well [60]. Figure 17a and 17b show a comparison of C-Mod data with the earlier and later scaling laws. The improvement in database conditioning also resulted in fits which were very close to being dimensionally correct without imposition of external constraints [61].

H-mode confinement can show considerable variability, even for plasmas with nominally similar control parameters. A series of experiments on C-Mod was performed to investigate this phenomenon [21]. Perhaps the most important “hidden variable” for H-mode performance on C-Mod is the level of radiated power. Figure 18 shows the confinement enhancement (H factor) relative to the ITER89 L-mode scaling for a set of discharges over a range of radiated power fraction, $f_{\text{RAD}} = P_{\text{RAD}}/P_{\text{TOT}}$. The confinement of L-mode discharges is found to be independent of f_{RAD} across the entire range of data, which includes, within experimental errors, $f_{\text{RAD}} = 1$. Part of the explanation for this is that much of the radiated power originates in the outer regions of the plasma and therefore substantial power is still conducted within the plasma interior. In contrast, H-mode confinement deteriorates when the radiated power fraction rises above 50%. As f_{RAD} approaches 1, the H factor also approaches 1; that is, strongly radiating H-mode show L-mode like confinement, though these discharges still have discernable, though small, edge pedestals. The role of marginal stability and critical gradients for this effect is discussed below in section 6. The effect of impurity radiation, particularly from the high-Z wall material, molybdenum, helps to explain the importance of the boronization treatment in achieving good quality H-modes in C-Mod [21]. Figure 19 shows a comparison of the radiated power profile for H-modes obtained before and after boronization. The sharp increase in absolute level and the shift of radiation into the core for the un-boronized discharge is dramatic. A similar story holds for neutral pressure

though the effects are not quite as clear cut. Good H-modes generally had divertor pressures below about 40mTorr and midplane pressures below about 0.3 mTorr. Another effect of the divertor is to allow the separatrix temperature to rise in H-mode by increasing the connection length to the first wall. Experiments on other devices had found that minimum gaps on the order of 1-2 cm between the separatrix and first wall were necessary to obtain good confinement [62]. On C-Mod, a scan of the outer gap distance showed no effect down to gaps of about 2mm (figure 20 [v]). This is approximately the scrape-off length for C-Mod [63]. H-modes obtained in limited discharges, that is with zero gap, had L-mode like confinement [64]. A final question addressed in these experiments was the requirement for high input power relative to L-H threshold power in obtaining good confinement. Figure 21 shows the confinement enhancement factor plotted against the ratio of input power to threshold power. The threshold power is taken from an early ITER scaling analysis [65]. While good confinement is obtained at powers close to threshold, one must understand that the threshold is computed based on parameters in the fully developed H-mode. That is, one must have a “reserve” of input power to account for the increase in density following the transition, typically a factor of 2-4, over the density of the target plasma.

5. Local Transport

Values of effective thermal diffusivity, χ , can be extracted via power balance analysis of the experimental data. The TRANSP code was used for this purpose as it has incorporated excellent physics modules for ICRF heating (TORIC) and fast-ion thermalization (FPPRF) [14, 66, 67].

Typical input data include profiles for electron density, electron temperature, Z_{EFF} , radiated power, total neutron rate and central ion temperature. The plasma boundary was calculated by the equilibrium reconstruction code EFIT [68]. For Ohmic plasmas in the linear confinement regime, the power was all generated in the electron channel and conducted mainly through the electron channel. Neo-classical ion transport was sufficient to account for the much smaller levels of power conducted through that channel. Electron thermal diffusivity, χ_e rose from ~ 0.5 m^2/sec into the range 1-2 m^2/sec as the density was lowered, as seen in much earlier studies [15] and consistent with the observed drop in confinement. The transport channels could also be separated for relatively low density, high-temperature ICRF-heated L-modes ($n_e < 1.5 \times 10^{20}$) where $\chi_e \sim \chi_i = 0.2 - 1.2$ m^2/sec in the confinement zone, $r/a \sim 0.3-0.8$. The higher values corresponded to stronger heating, consistent with the degradation seen in global confinement with input power. In these cases, where significant ICRF power was deposited in the ions, they were moderately anomalous with $\chi_i/\chi_{\text{NC}} \sim 1-4$, though with substantial error bars due to uncertainty in the ion-electron energy exchange term. At higher densities, this uncertainty prevented the separation of the two channels and instead an effective diffusivity, $\chi_{\text{EFF}} \equiv Q/(n_e \nabla T_e + n_i \nabla T_i)$ was calculated (where $Q = Q_e + Q_i$ is the total conducted heat flux). Figure 22 shows a comparison of χ_{EFF} between L-mode and H-mode discharges with similar toroidal field, plasma current, density and power deposition profiles. The decrease in thermal diffusivity is consistent with the difference in global confinement and demonstrates that the improvement in H-mode confinement occurs across the entire profile, not only in the edge barrier. In general, values and variations in other transport channels, particles, impurities [3] and momentum [4], reflect variation in thermal transport. Particle transport was measured using a modulated gas puff technique, which allows separation of the diffusive and convective components. Figure 23

shows profiles of these transport coefficients for a typical L-mode discharge [8]. Studies showed that $D_e \sim \chi_{\text{EFF}} \sim 0.2 - 1.0$ for L-modes [69]. Analogous studies, using transient analysis of impurity content and self-generated plasma rotation yielded similar results for those channels [70, 71]. We note that coupling of transport channels is not universal; when ion transport is suppressed in low density Ohmic or pellet fueled “P-mode” plasmas, particle transport is also suppressed but not electron energy transport [16, 72].

Another approach to local transport is via predictive modeling. Physics based models have been run for C-Mod, using input data from the experiment for the equilibrium, heating and density profile and comparing the calculated temperature profiles with those from the experiment. (Theoretical understanding of particle or momentum transport is still too primitive to allow a meaningful comparison.) The models tested were IFS-PPPL [73], GLF-23 [74] and the multi-mode model [75]. These models were all built using results of turbulence simulations or analytic calculations to estimate transport coefficients across a wide range of plasma parameters. While these models benchmarked well against larger, lower-field devices [76], all models tended to under-predict the C-Mod profiles for both L and H-modes, typically by about 30-40% [77, 78, 79]. A typical comparison is shown in figure 24. A set of parameter scans and simulations was conducted to try to understand the discrepancy. The conclusion was that the source of the problem was in the linear computation of the critical gradient length for micro stability[80]. Nonlinear calculations of this parameter yielded better agreement and are discussed below in section 6.

6. Marginal Stability and the Connection Between Global Confinement and Edge Temperature

The correlation between H-mode performance and pedestal height can be demonstrated by plotting the confinement enhancement factor vs edge temperature as in figure 25 [21]. To avoid sensitivity to details of the pedestal profile, the position used for the edge temperature is the 95% flux surface, which is slightly inside the pedestal. What is remarkable about this figure is that it unifies almost the entire C-Mod confinement database (the exception being discharges with peaked density) including L-mode and a wide range of H-mode types and qualities. It shows the quantitative connection between edge and core transport and suggests a direct link between local and global transport. Since the density profiles are relatively flat for these discharges, the proportionality suggests a strong correlation between edge and average temperature. This is confirmed by figure 26 which shows a series of temperature profiles for L and H-mode discharges. The temperature axis is plotted on a log scale, emphasizing the self-similarity of the profiles. If the temperature is given anywhere, it is defined everywhere. These results are summarized in figure 27, where the core temperature gradient is plotted against edge temperature [21] and provides an explanation for the so-called “enhanced L-mode”[81]. In these discharges, high power, well above the normal L-H threshold, is applied to plasmas which are prevented from entering H-mode by their topology. The confinement improvement can be understood as a consequence of increasing the edge temperature by brute force without the aid of an edge transport barrier. Figure 28 shows a plot of the edge temperature vs power per particle. The benefit of the H-mode transport barrier is that it allows production of high edge temperatures with only modest heating. A direct demonstration of the tight coupling between edge and core

temperatures was also obtained in experiments in which radiating gases were puffed into developed H-modes [82]. Radiation was peaked at $r/a \sim 0.8$ with 90% of the radiated power outside this radius and thus there was almost no change to the power flux in the plasma core. The result was strong cooling of the pedestal and a corresponding decrease in core ∇T , as seen in fig. 29,

Two important points are made by this set of plots. First, the difference in core energy confinement and thermal diffusivity between L- and H-mode can be understood to arise almost entirely from the difference in boundary conditions for the core temperature, rather than as intrinsic properties of core confinement in the regimes. Of course, the presence of an edge transport barrier in H-mode makes it far easier to attain a high-temperature boundary. Second, the temperature scale length tends to be constant over a wide range of plasma conditions. This point is made clearly in figure 30, where the normalized gradient, defined as $R/L_T = R|\nabla T|/T$, is plotted against input power. This plot points out the inutility of thermal diffusivity in characterizing transport and suggests a different model for understanding these discharges – namely the paradigm of marginal stability. In this model, transport is dominated by strong turbulence which is so efficient at transporting energy that the discharge remains near the stability boundary for the growth of the modes which underlie the turbulence. This picture can help explain figure 18 where L-mode confinement is maintained even as the conducted power is severely reduced. Conventional analysis would find χ dropping to extraordinarily low levels, especially in the outer portions of the plasma. However, from the perspective of marginal stability, it can be seen as the result of a temperature profile resilience given by the stability threshold and a boundary condition at the separatrix which is robust with respect to input power.

Apparent anomalies in studies of heat pulse propagation are explainable in this context as well. It is well known that thermal diffusivity calculated from propagation of temperature perturbations typically exceeds the value calculated from power balance. In a set of C-Mod experiments this effect grew stronger as input power was increased by almost an order of magnitude, with L_T changing only slightly. This is precisely the effect expected from a marginal stability model.

Theory predicts, in fact, that the micro-stability boundary for ITG (Ion Temperature Gradient) turbulence, which should dominate in these types of discharges, corresponds to a threshold in R/L_T [73]. Marginal stability will be maintained, even at high power as long as the turbulence is capable of conducting the input power effectively. For drift-wave-like turbulence, the maximum power which can be carried scales like $n_i T_i \rho_i^2$ and is well above the power levels in the C-Mod (and most other) experiments. Careful modeling of C-Mod discharges using the gs2 code allowed quantitative comparisons between theory and experiment and helped to explain the inadequacy of early transport modeling as discussed above in section 5 [80].

While C-Mod pushed the range of parameter interpolation which was used to derive the models (particularly collisionality and magnetic shear), that does not seem to be the resolution of the problem. Bringing the predictions of these transport models into agreement with the experimentally measured temperature profiles would have required dropping the thermal diffusivity to unphysically low values. That is, the measured temperature gradient exceeded the predicted linear critical gradient by a wide margin. To investigate these matters, the gs2 code, which can solve the nonlinear gyrokinetic equations as an initial value problem in flux tube

geometry with full electromagnetic and electron dynamic effects, was employed. This analysis showed that the discrepancy could be explained by a nonlinear upshift in the critical gradient due to the excitation and stabilizing influence of zonal flows [83]. Figure 31 shows the results of these calculations in a plot of conducted power vs normalized temperature gradient. Rough agreement with the experiments can be achieved only by a nonlinear calculation which includes all the relevant physics. These studies uncovered some interesting aspects of the nonlinear saturation of ITG turbulence and zonal flow damping. An important role for non-collisional damping of zonal flows was demonstrated along with the importance of maintaining non-adiabatic electron physics in these calculations [80]. The upshift could be artificially increased via unphysical assumptions of non-adiabatic electrons or by realistic assumptions of kinetic electrons in the higher collisionality of C-Mod H-modes.

7. Impurity Transport

As noted above, the changes in confinement regimes are accompanied by changes in impurity transport. Using the laser blow-off technique [84], non-recycling, non-intrinsic impurities were injected into a variety of discharge types and their transport determined. Figure 32 compares the decay of injected impurities in these three discharge types [34, 70]. For L-modes, the impurity confinement time, τ_I was roughly equal to the energy confinement time, τ_E , and scaled in a similar fashion. In EDA or ELMy H-modes, τ_I rose to 2-3 $\times \tau_E$, while in ELM-free H-modes, τ_I was more than 10 $\times \tau_E$, often too long to measure accurately [21]. Figure 33 shows the rapid change in impurity particle transport for a discharge making a transition from

ELM-free to EDA H-mode. The impurity diffusivity, D_i , in the core of EDA/ELMy discharges was comparable to the energy diffusivity and the main-ion particle diffusivity, (in the range 0.4-0.8 m^2/sec). However the impurities were also subject to a strong inward pinch, perhaps ten times as large as that of the main ions. Detailed analysis of impurity transport can be found in reference [3, 70]. These differences were reflected in the confinement of intrinsic impurities as well. The change in radiated power following an ELM-free to EDA transition was shown in figure 8 and was due to a change in molybdenum confinement. A striking difference in impurity particle transport between regimes is also evident in the H-mode pedestals. An array of high-resolution soft x-ray detectors was used to measure the transport of impurities in the plasma edge [45]. Soft x-ray profiles were much narrower in ELM-free discharges than in those with EDA or ELMs though with a width increasing with triangularity and q_{95} for both types. This observation suggests a deeper connection between particle transport and the ELM-free/EDA boundary which scales in the same way and with the same parameters. Transient analysis of the profiles following a transition found that the location of the x-ray pedestal could be attributed to a strong inward pinch located near the top of the pedestal. A strong pinch is to be expected from neoclassical theory because of the steep ion density gradient in this region. However the cause of the difference in x-ray pedestal width was a change in impurity diffusivity, which rose from 0.01 m^2/sec in ELM-free to about 0.04 in the EDA discharges studied. These values are essentially identical to the D_{EFF} of the electrons as shown in figure 11. The difference in electron density profile between the regimes was not as marked however, perhaps reflecting the weaker collisional pinch expected for the main ions.

8. Dimensionless Identity, Similarity and Scaling Experiments

It may be possible to develop a better understanding and to improve capabilities for extrapolating that understanding to future devices by characterizing transport in terms of dimensionless parameters [85]. Two types of experiments have been carried out in this regard. First, in dimensionless “identity” experiments, discharges are run in devices of different size with all dimensionless quantities, that are believed relevant, matched. The dimensioned parameters will be quite different in each however. C-Mod can play an important role in such experiments as they require matching a small high-field device with a larger low-field one. These experiments are aimed at demonstrating the validity of the dimensionless scaling approach; that is, they attempt to determine if all the important parameters have been identified. In the second type of experiments, carried out in individual machines or between machines, all but one of the dimensionless parameters are matched, providing a relation between a dimensionless dependent variable and a single independent dimensionless parameter. These dimensionless “similarity” or “scaling” experiments may provide a more direct connection to the underlying plasma physics than scans of the engineering parameters. The dimensionless independent variables include geometric factors like inverse aspect ratio, ϵ , elongation, κ , and triangularity, δ , and the plasma parameters q , the safety factor, β , the normalized plasma pressure, ν^* , the normalized collision frequency and ρ^* , the inverse of the normalized plasma size. For transport studies, the commonly used dependent variables are $B\tau_E$, the confinement time normalized by the cyclotron frequency and χ/χ_B , the thermal diffusivity normalized to Bohm diffusion.

Matching all of the dimensionless plasma parameters in devices of different size is equivalent to matching plasma shape and the set of parameters nR^2 , $BR^{5/4}$, $TR^{1/2}$ and $IR^{1/4}$. Then, if the plasma behavior depends only on these dimensionless variables, the input power required will match $PR^{3/4}$. Note that this requirement leads to a surface power density on the smaller of the machines in the comparison to be a factor of $(R_{\text{large}}/R_{\text{small}})^{11/4}$ higher than in the large experiment, limiting the range over which such experiments can be carried out. L-mode identity experiments performed between C-Mod and DIII-D are summarized in Table II and sample profiles are shown in figure 34. The heating methods varied between the two machines, with C-Mod using ICRF and DIII-D heating with neutral beams. Power deposition was slightly more peaked for C-Mod, but the (normalized) integrated power, which is the quantity that enters into the transport calculations, is very similar. While the absolute value of the confinement time varied by almost a factor of 3, the properly normalized times agreed to within 10% [86], comparable to experimental uncertainties. Local analysis showed an excellent match ($\pm 30\%$) in the normalized thermal diffusivity calculated in the range $r/a = 0.3-0.9$. A coordinated set of dimensionless identity experiments carried out by C-Mod, ASDEX-U, DIII-D and JET showed similar agreement [87] for H-mode discharges. Table III summarizes the C-Mod-JET comparisons. The “correctness” of the dimensionless approach is such that even with a ratio of 55 in the power flux, a match in the normalized temperature profile was obtained. The near match in sawtooth frequency is also noteworthy. The success of these experiments suggest that at least for standard L- and H-mode plasmas, the dominant parameters which determine performance come from plasma physics. Atomic physics, which might be important in the plasma edge (and which can be crucial in determining core confinement) was apparently not a significant factor in these cases. Particle and momentum sources from the neutral beams did not

seem to have a dominant effect either. To further investigate a possible role for atomic physics, edge dimensionless identity experiments were carried out with DIII-D [36]. When the dimensionless parameters were matched at the top of pedestal the entire pedestal profile was seen to match (fig 35). Since the dimensionless parameters associated with atomic physics were not matched for these experiments, the results provide a prima facie case that plasma physics rather than neutral penetration or radiation determines the pedestal structure.

A series of experiments was carried out to measure the scaling of transport with ρ^* and v^* in C-Mod [77, 78]. To perform the ρ^* scans, the magnetic field was scanned from 2.6 T to 5.3T. Holding β and v^* constant requires plasma density to be scaled as $B^{4/3}$ and temperature as $B^{2/3}$. This takes substantially more power for the higher field discharge and limits the range of ρ^* possible in any single machine. Table IV gives parameters for a particular matched pair of H-mode discharges. Combining the results from a number of experiments gave $B\tau_E \propto \rho^{*-3.4\pm 1.0}$, that is a scaling somewhat stronger than gyro-Bohm. Scans in L-mode plasmas gave the Bohm-like scaling, $B\tau_E \propto \rho^{*-1.8\pm 0.6}$. In both cases the error bars are relatively large because of the narrow range in ρ^* . It is relatively easy to scan over a wide range in v^* while holding the dimensionless quantities fixed. For L-mode, the field and current were varied by a factor of two, from 2.6T to 5.3T, while the plasma density was kept constant. By applying higher powers to the high-field cases, the temperature was raised to 4 times that of the corresponding low-field cases, keeping β and ρ^* unchanged. The low-field discharge then has a collisionality 16 times that of the high-field plasma. Table V compares some representative quantities for a pair of matched H-mode discharges, with a somewhat smaller range in v^* . The results from a broader data set can be seen in figure 36, where the dimensionless energy confinement time is seen to

degrade at higher v^* as $B\tau_E \sim v^{*-1.0 \pm 0.2}$. Similar experiments carried out in L-mode plasmas yielded a weaker degradation with collisionality, $B\tau_E \sim v^{*-0.4 \pm 0.1}$. These results were at least superficially in agreement with theoretical models. Higher collisionalities have been predicted to damp zonal flows and thus increase the level of saturated turbulence [88].

9. Summary

Confinement in the low-density ($n_{e,q} < 4 \times 10^{20}/\text{m}^3$), linear Ohmic (Alcator) regime matched previously derived scaling laws. At higher densities, the density dependence saturated and confinement was equivalent to L-mode. For this regime and RF heated L-modes, confinement agreed well with the ITER89 scaling. H-mode data from C-Mod averaged well above the ITER93 and ITER94 H-mode laws, pointing out the risks in extrapolating these empirical fits. The difficulty likely arose because of the limited range and correlation between independent variables in the original database. Addition of C-Mod data improved the conditioning of the H-mode database; unconstrained fits performed after the inclusion of C-Mod data obeyed the Connor-Taylor relations which was not the case earlier. Unlike other experiments, C-Mod H-modes do not have large type I ELMs. Instead, the pedestal gradients are regulated by small ELMs or a continuous quasi-coherent mode. The latter regime has been dubbed EDA for enhanced $D\alpha$ and is quasi-steady, with good energy confinement and no impurity accumulation. EDA H-modes are prevalent at higher q , higher triangularity, higher collisionality and with lower ion mass. These dependences along with theoretical studies suggest that the QC mode is a form of resistive ballooning. With higher pedestal pressure gradients and lower collisionality, small

(likely type II) ELMs emerge and take over pedestal regulation from the QC mode. C-Mod temperature profiles were self-similar, with the gradient proportional to the temperature. This observation demonstrated the first quantitative link between edge temperatures, core temperature gradients and core confinement consistent with theoretical predictions of marginal stability to ITG turbulence near a critical gradient length. L- and H-modes thus have similar intrinsic transport properties but differ because the edge transport barrier allows the production of a high temperature edge boundary condition. C-Mod H-mode temperature profiles could not be predicted, initially, by existing theory based models. Nonlinear gyrokinetic simulations showed that the change in electron dynamics induced at the higher collisionality led to an increase in the upshift of the critical temperature gradient. Local transport studies demonstrated connections between transport channels, with energy, particle and momentum transport varying across regimes in similar ways. The ability to measure rotation dynamics in torque-free discharges led to the unexpected observation of strong, self-generated toroidal flows in C-Mod. These studies, combined with measurements of SOL flows and transport have led to a novel explanation for the ∇B effect on the L-H threshold, perhaps explaining a long-standing mystery. Dimensionless identity experiments, carried out in collaboration with DIII-D, ASDEX-U and JET confirmed this approach over the widest available range in machine sizes. Non-dimensional scaling of edge parameters showed that the pedestals scaled with the dimensionless variables of plasma physics not atomic physics. Dimensionless scaling experiments showed a strong improvement in confinement with the normalized gyro-size ($1/\rho^*$). Confinement was found to be Bohm-like in L-mode and gyro-Bohm-like in H-mode. These experiments also showed a strong degradation in confinement with collisionality in agreement with expectations of linear zonal flow damping.

References

- [1] P. Bonoli, et al., “Wave-particle studies in the IC and LH range of frequencies in Alcator C-Mod”, published in this issue.
- [2] N. Basse, et al., “C-Mod Diagnostics”, published in this issue.
- [3] J. Rice, et al., “Impurity transport in Alcator C-Mod plasmas”, published in this issue
- [4] J. Rice, et al., “Spontaneous toroidal rotation in Alcator C-Mod plasmas with no momentum input”, published in this issue.
- [5] J. W. Hughes et al., “Studies of the H-mode pedestal on Alcator C-Mod”, published in this issue.
- [6] C. Fiore, et al., “Internal Transport Barriers in Alcator C-Mod”, published in this issue.
- [7] R. Parker, M. Greenwald, S. Luckhardt, E. Marmor, M. Porkolab & S. Wolfe, Nucl. Fusion, **25**, 1127, 1985.
- [8] M. Greenwald et al., Phys. Plasmas, **2**, 2308, 1995.
- [9] C. Fiore, et al., Phys. Plasmas **11**, 2480, 2004.
- [10] D. Garnier, et al., "Formation and Evolution of Internal Transport Barriers in Alcator C-Mod", Proceedings of IAEA 16th International Conference on Plasma Physics and Controlled Nuclear Fusion Research, Montreal, Volume **1**, 907, 1997.
- [11] M. Greenwald, et al., Phys. Rev. Letters **53**, 352, 1984.
- [12] S. Wolfe, et al., Phys. Plasmas **12**, 56110-1, 2005.
- [13] R. Goldston, Plasma Phys. Control. Fusion, **26**, 87, 1984.
- [14] R. Hawryluk, in Physics of Plasmas Close to Thermonuclear Conditions (Proc. Course Varenna 1979), Vol. **1**, CEC Brussels, 19, 1980.

- [15] A. Gondhalekar, et al., "Study of the energy balance in Alcator", Proceedings of the Seventh International Conference on Plasma Physics and Controlled Nuclear Fusion, Innsbruck, Austria, 1978. Volume **1**, p. 199, 1979.
- [16] M. Greenwald, et al., "Studies of the Regime of Improved Particle and Energy Confinement Following Pellet Injection into Alcator C.", Proceedings of IAEA 11th International Conference on Plasma Physics and Controlled Nuclear Fusion Research, Kyoto, Volume **I**, 139 (1987)
- [17] P. Yushmanov, et al., Nucl. Fusion **24**, 1999, 1990.
- [18] J. Freidberg, et al., "Alcator C-Mod Proposal", MIT-PFC Report RR-85-18, (also DOE/ET-51013-158), 1985.
- [19] Y. Takase, et al., Plasma Phys. Control. Fusion **38**, 2215, 1996.
- [20] F. Ryter, et al., Plasma Phys. Control. Fusion **38**, 1279, 1996.
- [21] M. Greenwald, et al., Nucl. Fusion, **37**, 793, 1997.
- [22] J. Snipes et al., Phys. Plasmas **3** 1992, 1996.
- [23] J. Snipes, et al., Nucl. Fusion **34**, 1039, 1994.
- [24] A. Hubbard et al., Plasma Physics and Controlled Fusion, **40**, (1998), 689
- [25] A. Hubbard, et al., Plasma Phys. Control. Fusion **46**, A95, 2004.
- [26] P. Guzdar, et al., Phys. Plasmas **11**, 1109, 2004.
- [27] B. LaBombard, et al., Nucl. Fusion **44**, 1047, 2004.
- [28] M. Greenwald, et al., Nucl. Fusion **28**, 2199, 1988.
- [29] J. Rice, et al., Nucl. Fusion **38**, 75, 1998.
- [30] H. Zohm, Plasma Phys. Control. Fusion **38**, 1213, 1996.
- [31] J. Snipes, et al., Plasma Phys. Control. Fusion **38**, 1127, 1996.
- [32] J. Snipes, et al., Plasma Phys. Control Fusion **40**, 765, 1998.

- [33] P. Stek, “Reflectometry Measurements on Alcator C-Mod”, PhD. Thesis, MIT, 1997
- [34] M. Greenwald, et al., Phys. Plasmas, **6**, 1943, 1999.
- [35] M. Bures, et al., Nucl. Fusion **32**, 539, 1992.
- [36] Mossessian, D.A. et al., Physics of Plasmas, **10**, 689, 2003.
- [37] K. Kamiya, et al, Plasma Phys. Control. Fusion **46**, 1745, 2004.
- [38] K. McCormick, et al., Jour. Nucl. Mat **337-339**, 520, 2005.
- [39] S. Mirnov, et al., Nuclear Fusion, **39**, 2251, 1999.
- [40] M. Greenwald, et al., Plasma Phys. Control. Fusion **42**, A263, 2000.
- [41] Y. Kamada, et al, Plasma Phys. Control. Fusion **42**, A247, 2000.
- [42] D. Mossessian, et al., Plasma Phys. Control. Fusion **44**, 423, 2002.
- [43] D. Mossessian, et al., Phys. Plasmas **10**, 1720, 2003.
- [44] H. R. Wilson, P. Snyder, et al., Phys. Plasmas **9**, 1277, 2002.
- [45] T. Sunn Pedersen, et al., Nucl. Fusion **40**, 1795, 2000.
- [46] J. Snipes, et al., Plasma Phys. Control. Fusion **43**, L23, 2001.
- [47] N. Basse, et al., Phys. Plasmas **12**, 52512-1, 2005
- [48] A. Mazurenko, et al., Phys. Rev. Letters **89**, 225004-1, 2002.
- [49] A. Hubbard, et al., Phys. Plasmas **8**, 2033, 2001.
- [50] R. Slusher, et al., Phys. Rev. Letters **53**, 667, 1984.
- [51] G. Tynan, Phys. Plasmas **1**, 3301, 1994.
- [52] R. Moyer, et al, Jour. Nucl. Mat., **266-269**, 1145, 1999.
- [53] B. Rogers, J. Drake, Phys. Plasmas **6**, 2797, 1999.
- [54] L. Garcia, B. Carreras, V. Lynch, Phys. Plasmas **6**, 107, 1999.
- [55] B. Rogers, J. Drake, A. Zeiler, Phys. Rev. Lett **81**, 4396, 1998.

- [56] X. Xu, Phys. Plasmas **7**, 1951, 2000.
- [57] W. Nevins, et al., “Simulations of boundary turbulence in tokamak experiments”, *Proceedings of 19th Conference on Fusion Energy*, Lyon, 2002. (available at http://www-pub.iaea.org/MTCD/publications/PDF/csp_019c/pdf/thp3_07.pdf)
- [58] W. Dorland, F. Jenko, M. Kotschenreuther, and B.N. Rogers, Phys. Rev. Lett. **85**, 5579, 2000.
- [59] ITER H Mode Database Working Group, Nucl. Fusion, **34**, 131, 1994.
- [60] ITER Expert Groups on Confinement, Transport, Confinement Modeling and Databases, Nucl. Fusion **39**, 2175, 1999.
- [61] J. G. Cordey, et al., Plasma Physics and Controlled Fusion, **39**, B115, 1997.
- [62] ASDEX Team, Nucl. Fusion **29**, 1959, 1989.
- [63] B. LaBombard, J. Nucl. Mater. **241-243** (1997) 149.
- [64] B. LaBombard, Phys. Plasmas **12** (2005) 056111.
- [65] Snipes J et al., Proc. 24th EPS (Berchtesgaden) vol **21A**, part II, p 565, 1997.
- [66] M. Brambilla, Plasma Phys. Control. Fusion, **41**, 1, 1999
- [67] G. Hammett, “Fast Ion Studies of Ion Cyclotron Heating in the PLT Tokamak”, PhD Thesis Princeton Univ., 1986.
- [68] L. Lao, et al., Nucl. Fusion **25**, 1611, 1985.
- [69] T. Luke, “Measurement of particle transport coefficients on Alcator C-Mod” MIT PhD. Thesis, 1994.
- [70] J. Rice, et al., Phys. Plasmas **4**, 1605, 1997.
- [71] W.D. Lee, et al, Phys. Rev. Letters **91**, 205003/1, 2003.
- [72] S. Wolfe, et al., Nucl. Fusion **26**, 329, 1986.

- [73] M. Kotschenreuther, W. Dorland, M. Beer, G. Hammett, *Phys. Plasmas* **2**, 2381, 1995.
- [74] R. Waltz, et al., *Phys. Plasmas* **4**, 2483, 1997.
- [75] G. Bateman, et al., *Phys. Plasmas* **5**, 1793, 1998.
- [76] D. Boucher, et al., *Nucl. Fusion*, **40**, 1955, 2000.
- [77] J. Schachter, "Local Transport Analysis for the Alcator C-Mod Tokamak", MIT PhD Thesis, 1997.
- [78] M. Greenwald, et al., *Plasma Phys. Control. Fusion* **40**, 789, 1998.
- [79] A. Pankin, et al., *Phys. Plasmas* **8**, 4403, 2001.
- [80] D. Mikkelsen, et al., "Nonlinear Simulations of Drift-Wave Turbulence in Alcator C-Mod", *Proceedings of 19th Conference on Fusion Energy*, Lyon, 2002.
- [81] F. Ryter, et al., *Plasma Phys. Control. Fusion* **40**, 725, 1998.
- [82] A. Hubbard, et al., *Proceedings of the 26th EPS Conf. on Contr. Fusion and Plasma Physics*, Maastricht, 14 - 18 June 1999 ECA Vol. **23J**, 13, 1999.
- [83] A. Dimits, et al., *Phys. Plasmas* **7**, 969, 2000.
- [84] E. Marmor, J. Cecchi, S. Cohen, *Rev. Sci. Instrum.* **46**, 1149, 1975.
- [85] J. Connor, J. Taylor, *Nucl. Fusion* **17**, 1047, 1977.
- [86] T. Luce, et al., *Nucl. Fusion* **42**, 1193, 2002.
- [87] J. Christiansen, et al., "Experimental tests of confinement scale invariance on JET, DIII-D, AUG, and C-Mod", *Proceedings of IAEA 17th International Conference on Plasma Physics and Controlled Nuclear Fusion Research*, Yokohama (1998), Vol. **2**, 765, 2000.
- [88] M. Rosenbluth and F. Hinton, *Phys. Rev. Letters* **80**, 724, 1998.

Figure Captions

1. The energy confinement time, τ_E , is plotted against density for discharges with Ohmic heating alone. The dependence on elongation is in part a manifestation of the q scaling in the linear regime. For standard plasma shapes, $k \sim 1.5$ or higher, the linear confinement (Alcator) regime is obtained only at densities below $\sim 6 \times 10^{20}$.

2a. A power law regression for confinement data from the linear Ohmic confinement regime (LOC).

2b. Ohmic confinement data is plotted against the neoAlcator scaling law. Reasonable agreement is obtained in the low density regime. The blue and red points correspond to a set of dedicated scans.

3a. A power law regression for confinement data from the saturated Ohmic confinement regime (SOC).

3b. Ohmic confinement data from the SOC regime is plotted against the predictions of the ITER89 L-mode scaling law.

4a. A power law regression of C-Mod L-mode confinement data shows the strong scaling with plasma current and input power which is typical of that regime.

4b. The L-mode data is compared with the ITER89 L-mode scaling law.

5. A comparison of ELM-free and EDA discharges. The only significant difference in the target plasmas is the slightly lower target density for the ELM-free case. However, a sharp drop in particle confinement is inferred the density and radiated power traces for EDA. The result is a steady discharge with good energy confinement.

6. At higher pedestal pressures, small ELMs can be seen superimposed on the EDA plasmas. While individual ELMs are visible on $H\alpha$ and divertor probes (I_{SAT}), no drop in global stored energy or line averaged density can be discerned.

7a. The dependence of the ELM-free EDA boundary can be seen in this triangularity scan. As δ is lowered, the discharge begins to dither between these two H-mode regimes, finally, as seen by the radiated power curve, losing its H-mode character.

7b. On this expanded scale, it can be seen that each dither from ELM-free to EDA is a complex structure consisting of a series of QC fluctuation bursts, each lasting about 0.5 msec.

8. An EDA H-mode is obtained with Ohmic heating alone. The transition from ELM-free to EDA, which was the result of raising q_{95} via a B_T scan, occurs at about 1.0 sec. and is accompanied by an decrease in impurity content, a drop in the rate of density rise and the appearance of the QC mode.

9. The EDA ELM-free boundary is plotted in q - δ space showing that EDA is more likely at higher safety factor and higher triangularity. There are significant areas of overlap suggesting that other variables are important as well.

10. The boundary between EDA and small, type II ELMs is plotted in a space comprised of the edge temperature and the normalized pressure gradient (α_{MHD}). EDA tends to disappear at higher pressures and temperatures. The square symbols denote shots for which MHD stability calculations have been performed. The boundary between regimes seems to be coincident with the stability boundary for intermediate n peeling-ballooning modes.

11. The effective pedestal particle diffusivity, D_{EFF} (calculated at the separatrix) is plotted vs the amplitude of the QC mode. The near-linear relation suggests a causal relationship between the mode and enhanced particle transport.

12. The QC mode autopower spectra are plotted for data from the PCI and Reflectometry diagnostics.

13. The evolution of the QC mode spectra showing strong downward sweeps in frequency following each transition can be seen in a discharge with three distinct H-mode periods,. The change in frequency is believed to be from Doppler shifts which arise as rotation builds up in the pedestal.

14. Wavenumber resolved spectra of the QC mode from the PCI diagnostic show well defined mode structures. The positive and negative features correspond to the top and bottom of the machine which are traversed by the PCI beam.

15. The wavenumber of the QC mode from a number of diagnostics, compared to the predictions for a field aligned perturbation, show good agreement.

16. The QC mode amplitude, taken from scanning probe data, is plotted vs radius. From this measurement, a mode width of 1-2mm is inferred. The shaded region represents the separatrix with uncertainty from the equilibrium mapping.

17a. H-mode confinement data from C-Mod are significantly above the predictions of the ITER93 ELM-free scaling law, which was derived prior to C-Mod operation. Note that the scaling line should be compared primarily to the red circles.

17b. After C-Mod data were added to the international database and the regressions recalculated, the agreement improved. Note that the scaling line should be compared primarily to the green squares.

18. The confinement enhancement factor H_{ITER89} is plotted against $f_{\text{RAD}} \equiv P_{\text{RAD}}/P_{\text{TOTAL}}$ for both L and H-mode discharges. The L-mode confinement is seen to be insensitive to this parameter while confinement in the H-mode plasmas drops when f_{RAD} rises above 0.5.

19. Profiles of radiated power taken before and after boronization, indicate a dramatic drop in high-Z impurity content following the wall treatment.
20. The H factor is plotted vs outer gap, showing that confinement does not deteriorate if the plasma wall spacing is larger than 2-3 mm. This distance roughly corresponds to the scrape-off layer width. H-modes were not obtained in discharges limited on the outer wall.
21. The H factor is plotted vs $P/P_{\text{THRESHOLD}}$. Good confinement is achieved if the heating power is at the threshold computed for the fully developed H-mode. It is important to note that this level of input power is two to four times the threshold power as computed for the target plasma.
22. The effective thermal diffusivity, χ_{EFF} , is compared between a matched L-mode and H-mode pair of discharges. The discharges had the same shape, I_p , B_T , P_{RF} and n_e . The L-mode discharge was taken with reversed field to suppress the transition, despite the strong heating.
23. Particle transport coefficients, calculated from the plasma response to a set of gas puffs, are plotted vs radius. Note that thermal and particle diffusivity are similar in value.
24. Measured T_e profiles were found to be significantly above those predicted by several physics-based models. The discrepancy was apparently resolved by nonlinear turbulence calculations. (The upturn in the predicted T_e profiles near the magnetic axis can be attributed to the lack of sawteeth in the models.)

25. The confinement enhancement factor, H is seen to be tightly correlated with the pedestal temperature across confinement regimes.

26. Temperature profile self-similarity (with the local gradient proportional to the local value) is demonstrated here in a semi-log plot of profiles using data from 100 shots chosen randomly from the 2003 and 2004 experimental campaigns. The data were restricted to steady, sawtooth discharges at 1MA and 5.3T, to hold the magnetic shear approximately constant. For consistency, data is plotted at the top of each sawtooth nearest the random time chosen. Otherwise the data contains all powers, plasma densities and are a mixture of L and H-modes. (Colors are employed to aid in following particular profiles but are otherwise arbitrary.)

27. The core temperature gradient is also seen to be tightly correlated with pedestal temperature, accounting for the increase in stored energy and confinement.

28. The pedestal temperature is plotted vs power per particle. Following the results seen in figures z, aa and bb, the principal difference between core transport in L-mode and H-mode is the ease with which high edge temperatures are obtained in the latter regime.

29. A direct demonstration of the tight connection between edge and core temperatures was obtained in experiments in which radiating gases were puffed into developed H-modes. Radiation was peaked at $r/a \sim 0.8$, and resulted in a strong cooling of the pedestal. A corresponding decrease in core ∇T was observed, despite the fact that 90% of the radiated power

was outside this radius. As in the global dataset, the temperature scale length L_T remained constant

30. The normalized temperature gradient, R/L_T is plotted vs input power. The constancy of the gradient is consistent with marginal stability and the predictions of the critical gradient for ITG modes from theory.

31. Results of a detailed calculation of the critical gradient are shown. The experimental heat flux and gradient are consistent with the nonlinear computation. The upshift in critical gradient in the calculation is due to stabilization of ITG turbulence by zonal flows. This result helps to explain the discrepancy seen in figure y.

32. The brightness of niobium impurity lines following injection into two different discharges. After a brief influx phase, the impurity accumulated in an ELM-free discharge, but not in the EDA discharge. The ELM-free H-mode was transient and following its return to L-mode at 0.973 sec, the rapid loss of the impurity was apparent.

33. The difference in impurity confinement between the H-mode regimes is clear in this discharge where scandium was injected into a developed ELM-free plasma which later made a spontaneous transition to EDA at 0.86 sec. The long impurity confinement time in the ELM-free phase contrasts with the decreased particle confinement in the EDA phase which followed.

34. Appropriately scaled plasma profiles are shown for two discharges in a dimensionless identity comparison of C-Mod and DIII-D. Reasonable matches were obtained across the profiles. The largest difference was the somewhat more peaked power deposition obtained with ICRF heating on C-Mode compared to the NBI heating on DIII-D. Since it is the integrated power flux which enters the transport calculations, this difference is not believed to be important over most of the plasma.

35. A pair of dimensionless pedestal comparisons, from C-Mod and DIII-D, show that the entire profile could be matched, suggesting a primary role for plasma physics in determining the edge profiles.

36. An example of dimensionless scaling, in which the normalized confinement time is plotted against collisionality with all other dimensionless parameters (β , ρ^* , ϵ , δ , κ , etc) held constant. The decrease in confinement at higher collisionality is consistent with predictions from theories of collisional damping of zonal flows.

Table Captions

I. Summary of EDA and ELM-free H-mode features [723].

II. Parameters from dimensionless comparison C-Mod and DIII-D L-modes [86].

III. Parameters from dimensionless identity comparison C-Mod and JET H-modes [87].

IV. Parameters for dimensionless ρ^* scaling experiment on C-Mod [77].

V. Parameters for dimensionless v^* scaling experiment on C-Mod [77].

Table I. Summary of EDA and ELM-free H-mode features

	ELM-free H-mode	EDA H-mode
Energy Confinement	$H_{89} \sim 2.1$	$H_{89} \sim 1.9$
Particle Confinement	$\tau_I \gg \tau_E$	$\tau_I \sim 2-3 \times \tau_E$
Momentum Confinement	Strong inward pinch	diffusive
Edge Fluctuations	None observable	Quasi-coherent fluctuations 50-200 kHz
X-ray Pedestals	Narrow, 2-6 mm	Wide, 4-12 mm
Dependence on q_{95}	More likely when $q_{95} < 3.7$	More likely when $q_{95} > 3.7$
Dependence on δ	$\delta < 0.35$	$0.35 < \delta$
Dependence on density, collisionality	Favored at low density and collisionality	Favored at high density and collisionality

Table II. Parameters from dimensionless comparison C-Mod and DIII-D L-modes.

	C-Mod	DIII-D
Engineering		
B (T)	5.22	1.61
a (m)	0.22	0.57
n_e ($10^{20}/\text{m}^3$)	1.80	0.26
P_{TOT} (MW)	3.2	1.9
τ_E (sec)	0.027	0.079
Dimensionless		
R/a	3.07	3.06
$Ba^{5/4}$	0.79	0.79
na^2	0.85	0.82
β_{th} (%)	0.51	0.52
q_{95}	3.6	3.7
$B\tau_E$ (T s)	0.141	0.127

Table III. Parameters from dimensionless identity comparison C-Mod and JET H-modes.

	C-Mod	JET
$10^4 \rho^*$	2.7	2.8
$10^3 v^*$	123	147
β_N	0.9	1.3
q_{95}	3.3	2.7
$B\tau_E$ (T s)	0.31	0.31
f_{ELM}	0	0
$f_{Sawtooth}$	9	11

Table IV. Parameters for dimensionless ρ^* scaling experiment in C-Mod H-modes.

Shot	960118016	960130020
Engineering		
B_T (T)	2.5	5.4
I_P (MA)	0.5	1.1
n_e ($10^{20}/\text{m}^3$)	1.38	2.90
P_{RF} (MW)	0.92	2.01
Dimensionless		
β_T (%)	1.10	1.03
q_{95}	3.26	3.23
v^*	0.54	0.40
T_i/T_e	0.87	1.01
P_{RAD}/P_{TOT}	0.18	0.13
$1000\rho^*$	6.24	4.21
$B\tau_E$ (T s)	0.06	0.22

Table V. Parameters for dimensionless v^* scaling experiment on C-Mod

Shot	960118030	960130020
Engineering		
B_T (T)	2.6	5.3
I_P (MA)	0.6	1.1
n_e ($10^{20}/\text{m}^3$)	2.25	2.6
P_{RF} (MW)	0.93	1.99
Dimensionless		
β_T (%)	1.28	1.14
q_{95}	3.24	3.19
$1000\rho^*$	4.90	4.68
T_i/T_e	0.92	1.0
P_{RAD}/P_{TOT}	0.11	0.08
v^*	1.10	0.23
$B\tau_E$ (T s)	0.06	0.30

Fig. 1. The energy confinement time, τ_E , is plotted against density for discharges with Ohmic heating alone. The dependence on elongation is in part a manifestation of the q scaling in the linear regime. For standard plasma shapes, $k \sim 1.5$ or higher, the linear confinement (Alcator) regime is obtained only at densities below $\sim 6 \times 10^{20}$.

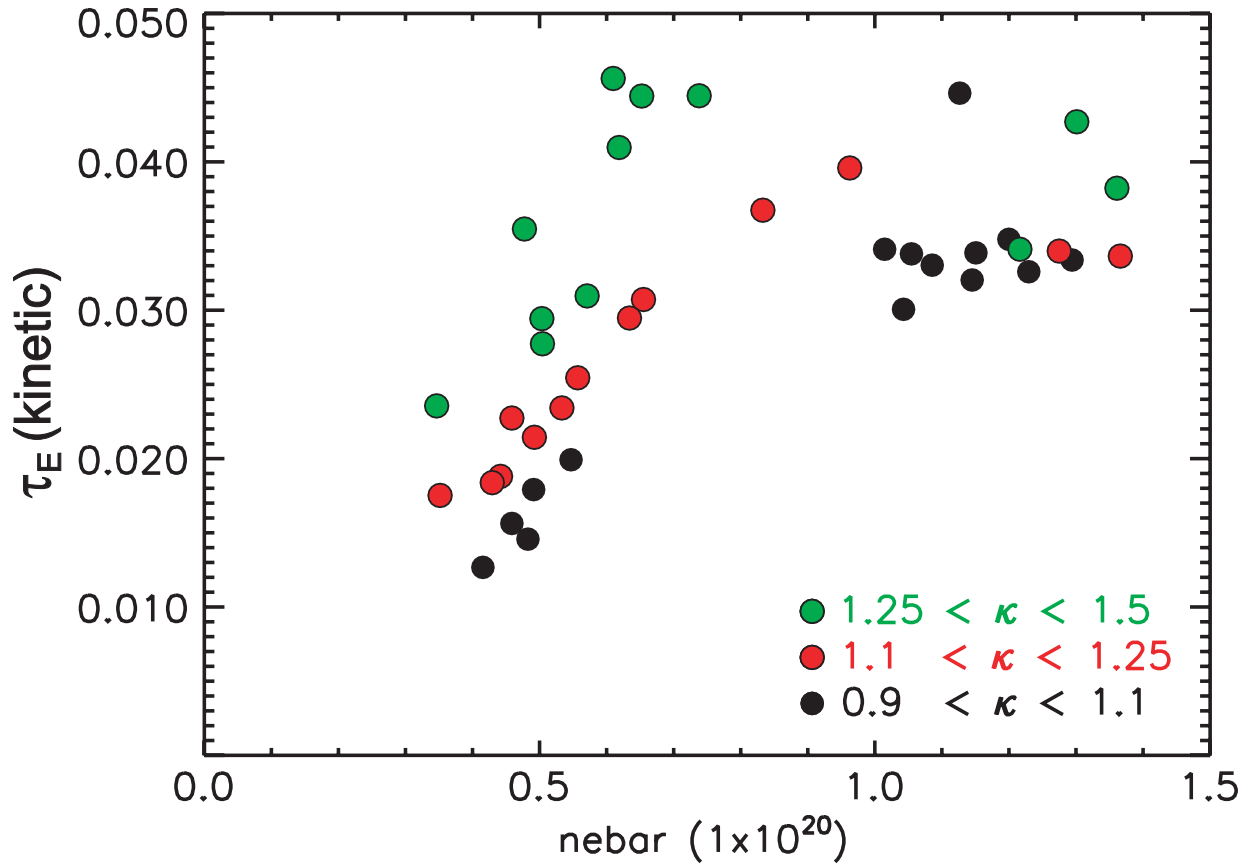


Fig. 2a. A power law regression for confinement data from the linear Ohmic confinement regime (LOC).

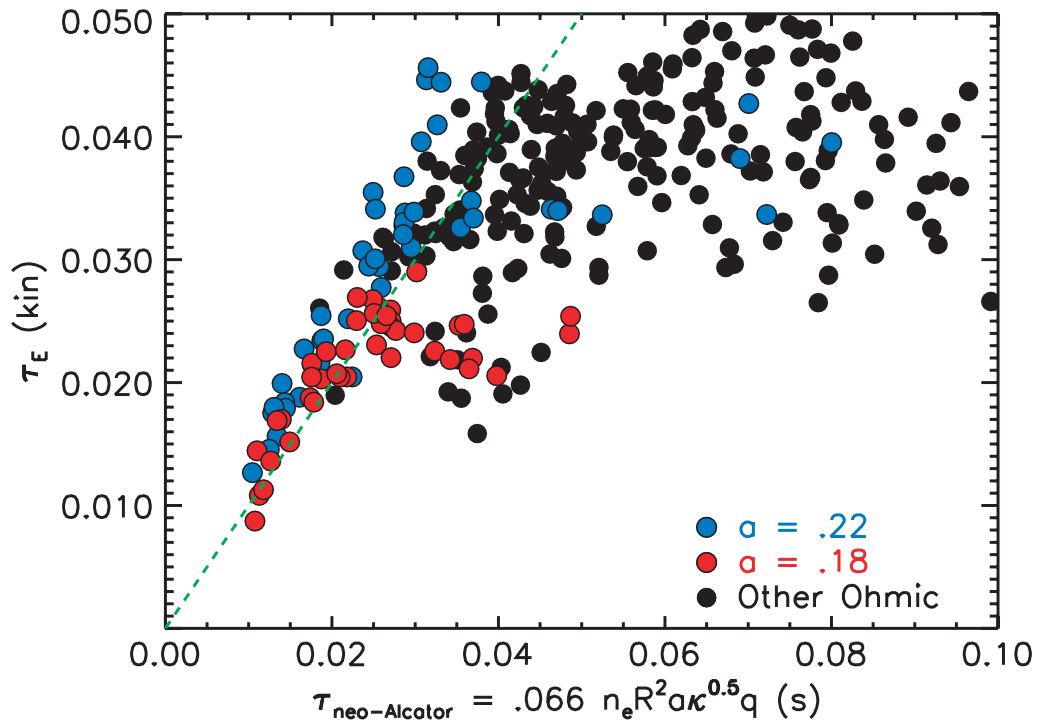
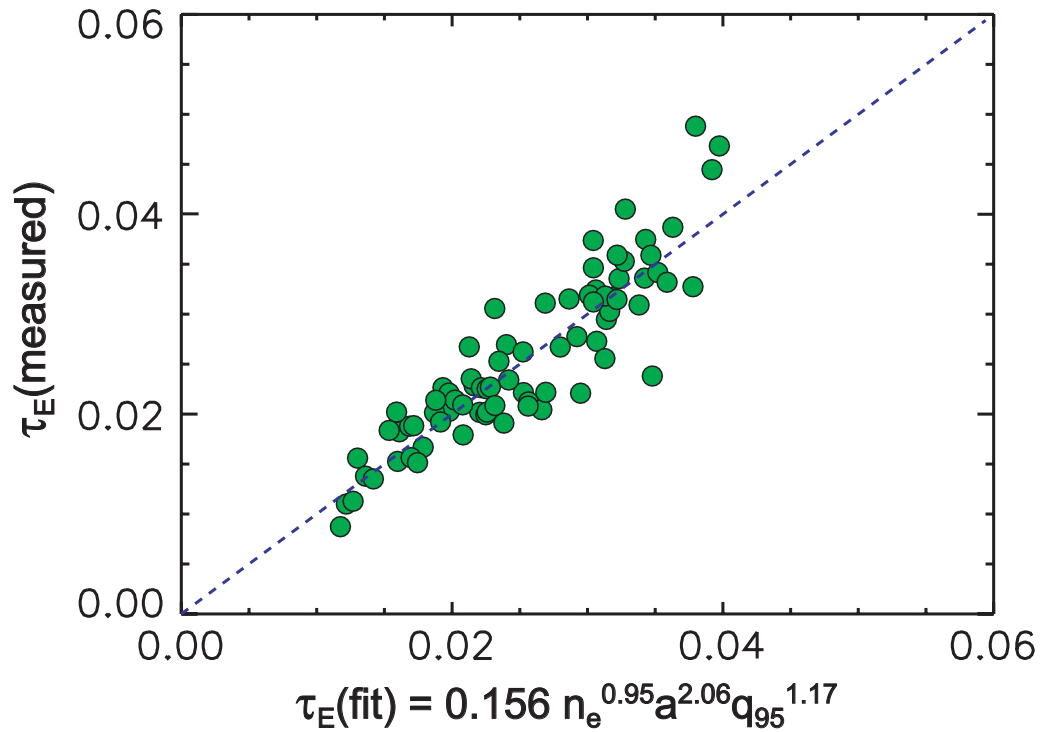


Fig. 2b. Ohmic confinement data is plotted against the neoAlcator scaling law. Reasonable agreement is obtained in the low density regime. The blue and red points correspond to a set of dedicated scans.

Figure 3a. A power law regression for confinement data from the saturated Ohmic confinement regime (SOC).

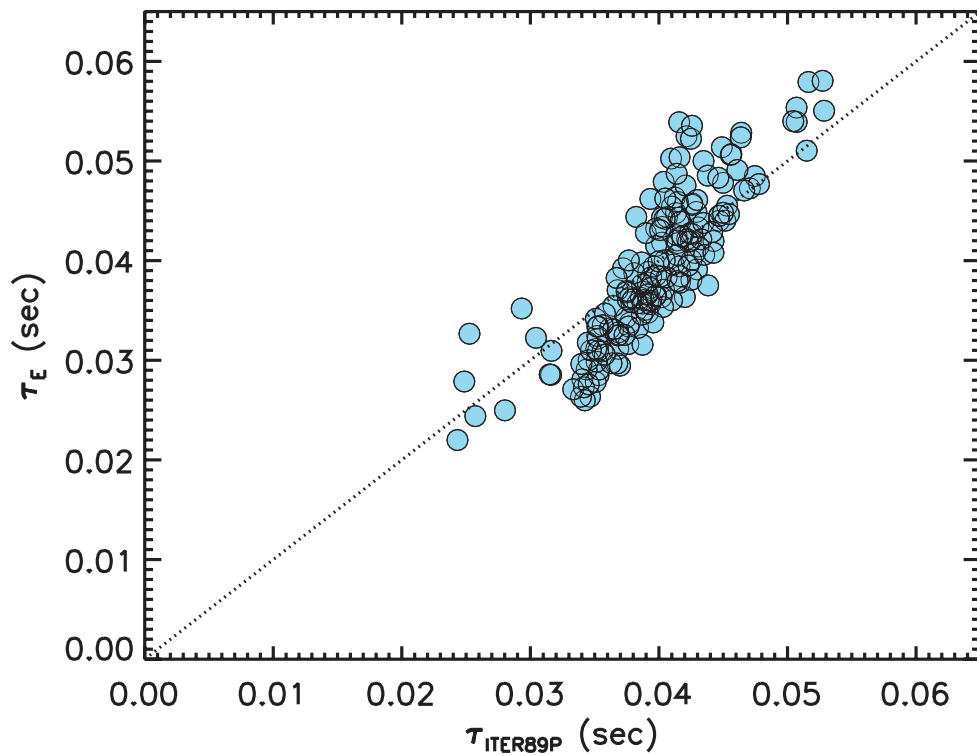
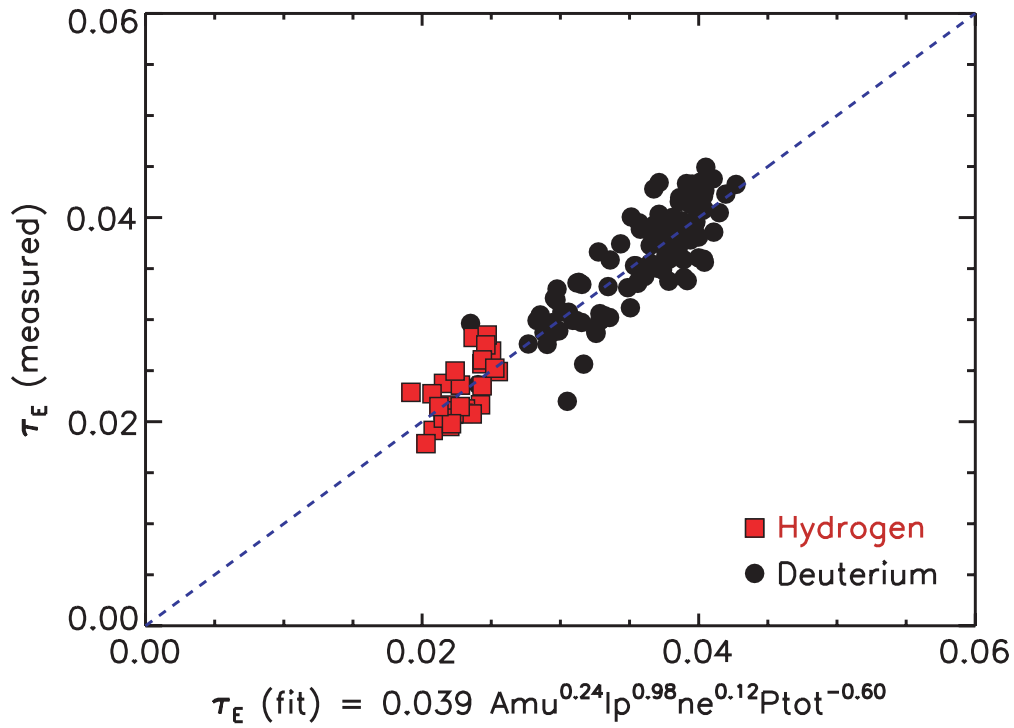


Figure 3b. Ohmic confinement data from the SOC regime is plotted against the predictions of the ITER89 L-mode scaling law.

Figure 4a A power law regression of C-Mod L-mode confinement data shows the strong scaling with plasma current and input power which is typical of that regime.

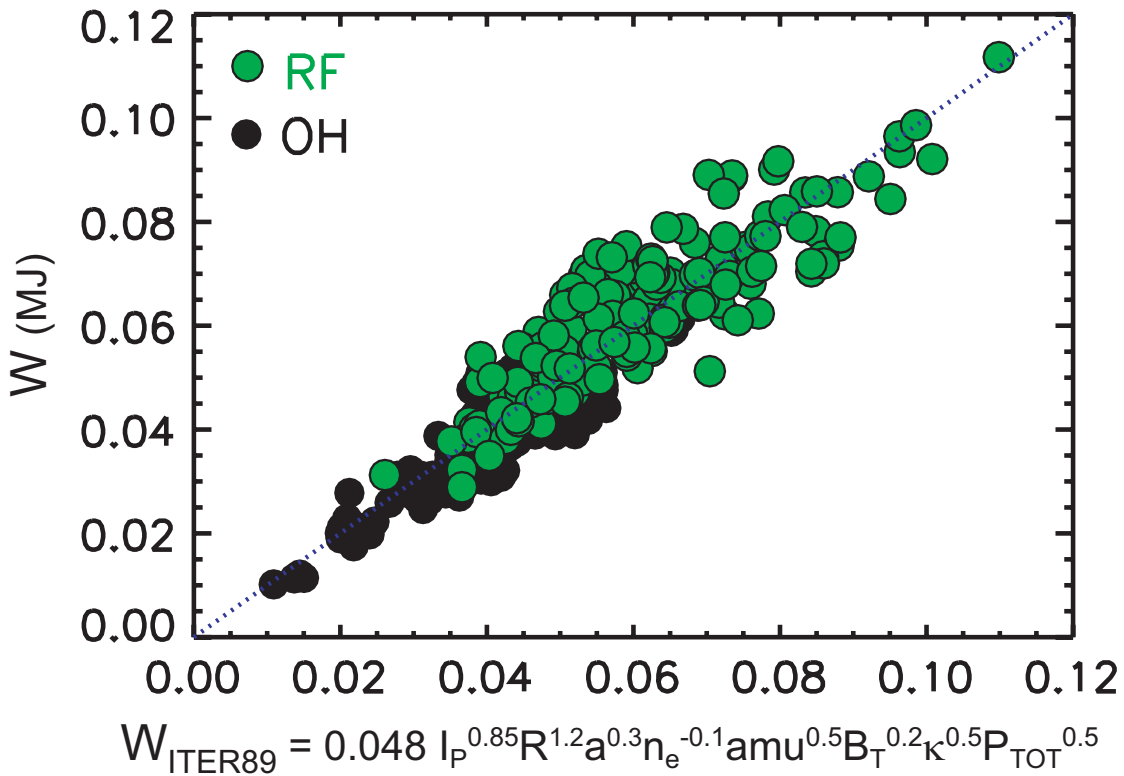
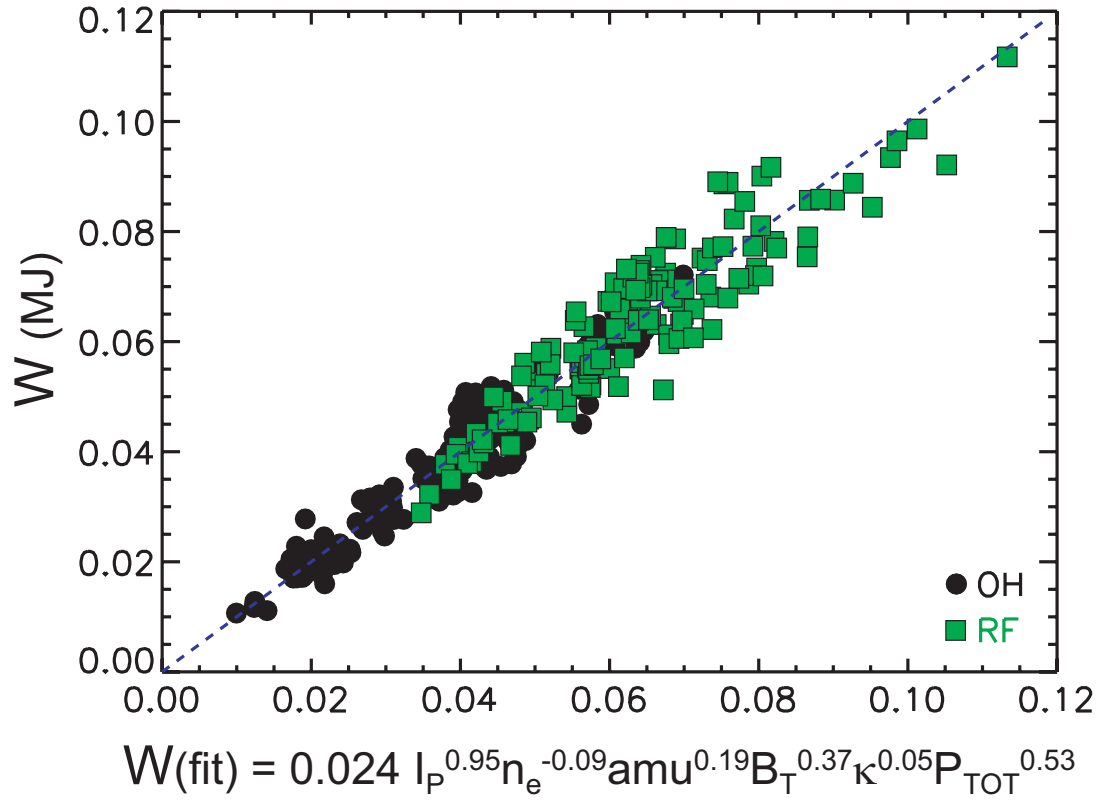


Figure 4b The L-mode data is compared with the ITER89 L-mode scaling law.

Figure 5. A comparison of ELM-free and EDA discharges. The only significant difference in the target plasmas is the slightly lower target density for the ELM-free case. However, a sharp drop in particle confinement is inferred the density and radiated power traces for EDA. The result is a steady discharge with good energy confinement.

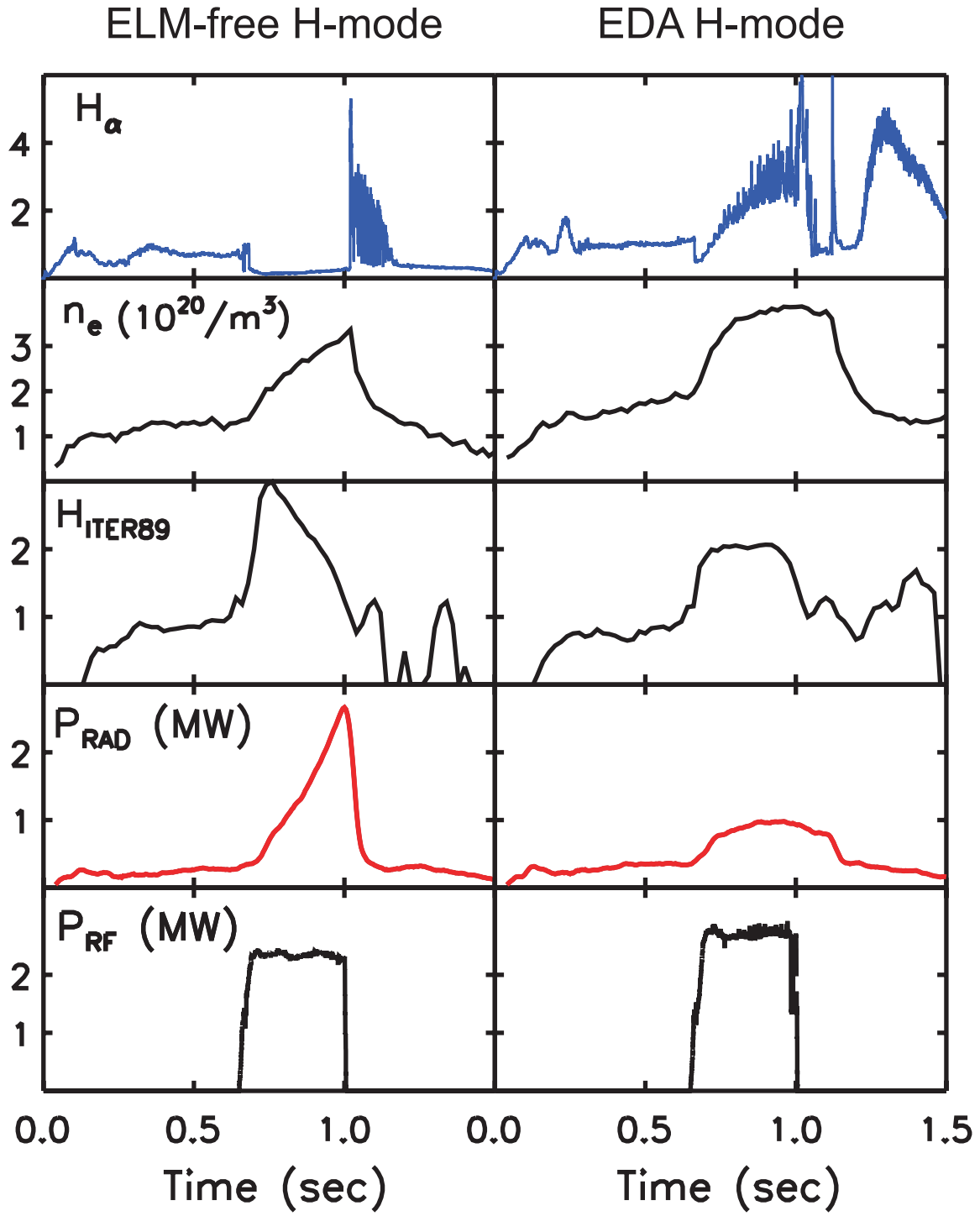


Figure 6. At higher pedestal pressures, small ELMs can be seen superimposed on the EDA plasmas. While individual ELMs are visible on $H\alpha$ and divertor probes (I_{SAT}), no drop in global stored energy or line averaged density can be discerned.

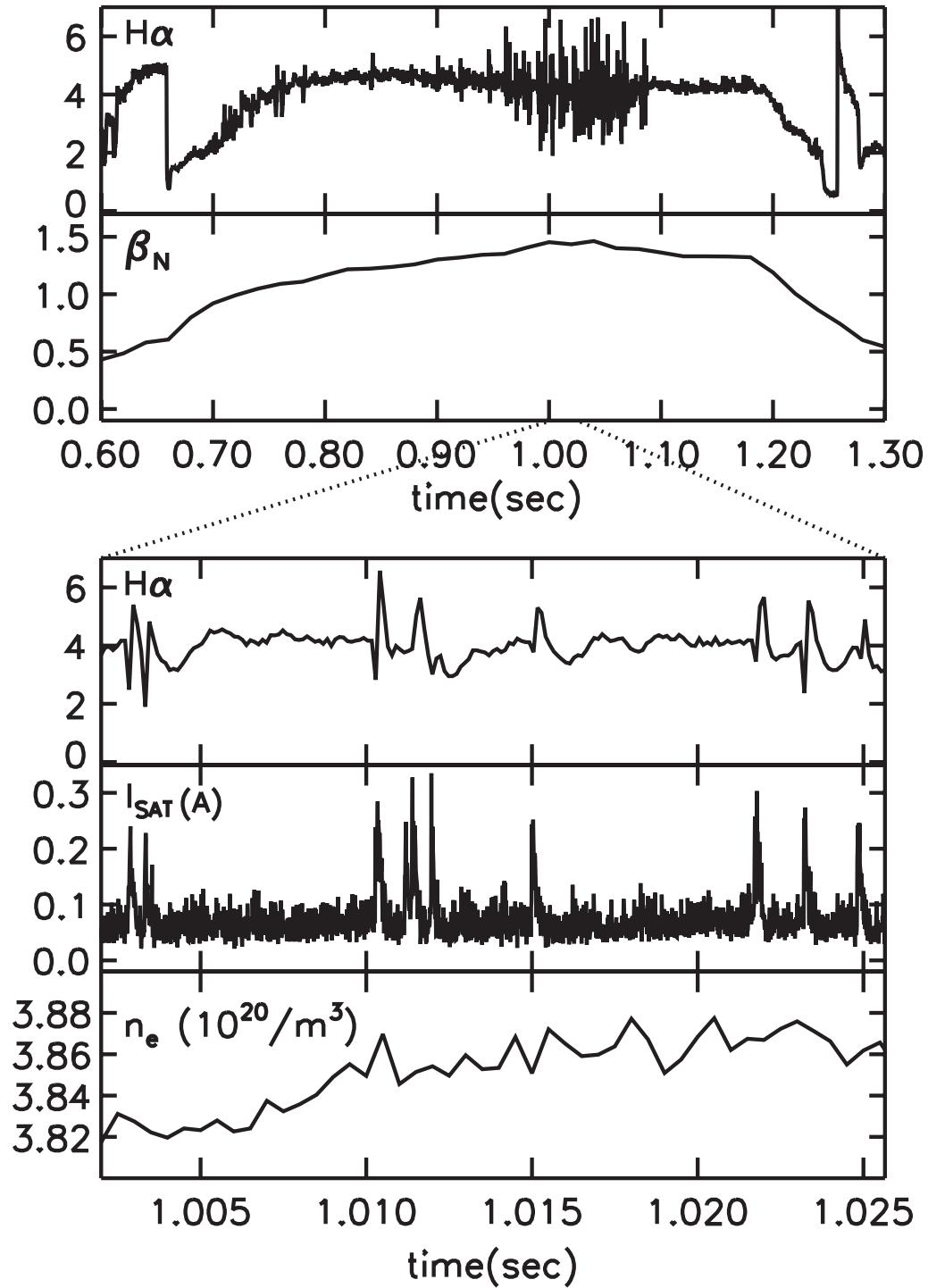


Figure 7a. The dependence of the ELM-free EDA boundary can be seen in this triangularity scan. As δ is lowered, the discharge begins to dither between these two H-mode regimes, finally, as seen by the radiated power curve, losing its H-mode character.

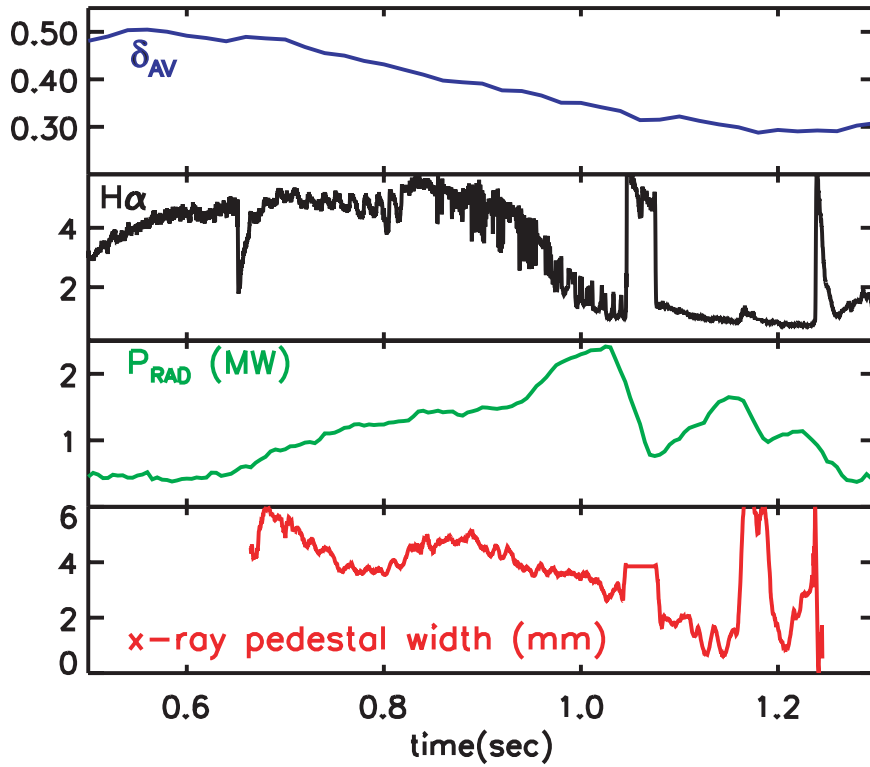


Figure 7b. On this expanded scale, it can be seen that each dither from ELM-free to EDA is a complex structure consisting of a series of QC fluctuation bursts, each lasting about 0.5 msec.

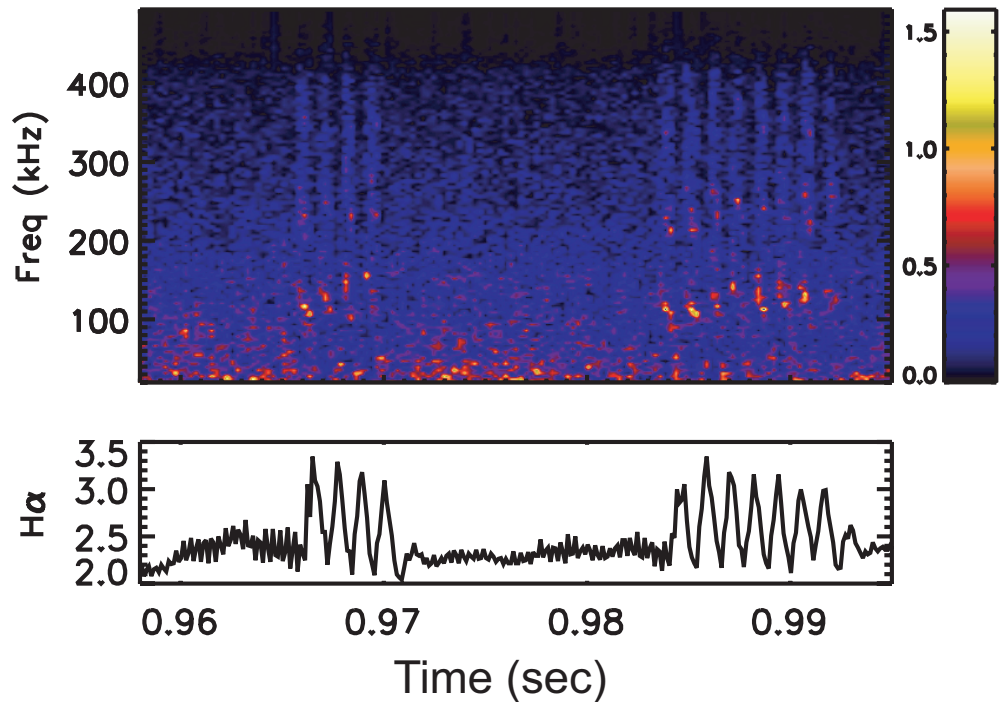


Figure 8. An EDA H-mode is obtained with Ohmic heating alone. The transition from ELM-free to EDA, which was the result of raising q_{95} via a B_T scan, occurs at about 1.0 sec. and is accompanied by an decrease in impurity content, a drop in the rate of density rise and the appearance of the QC mode.

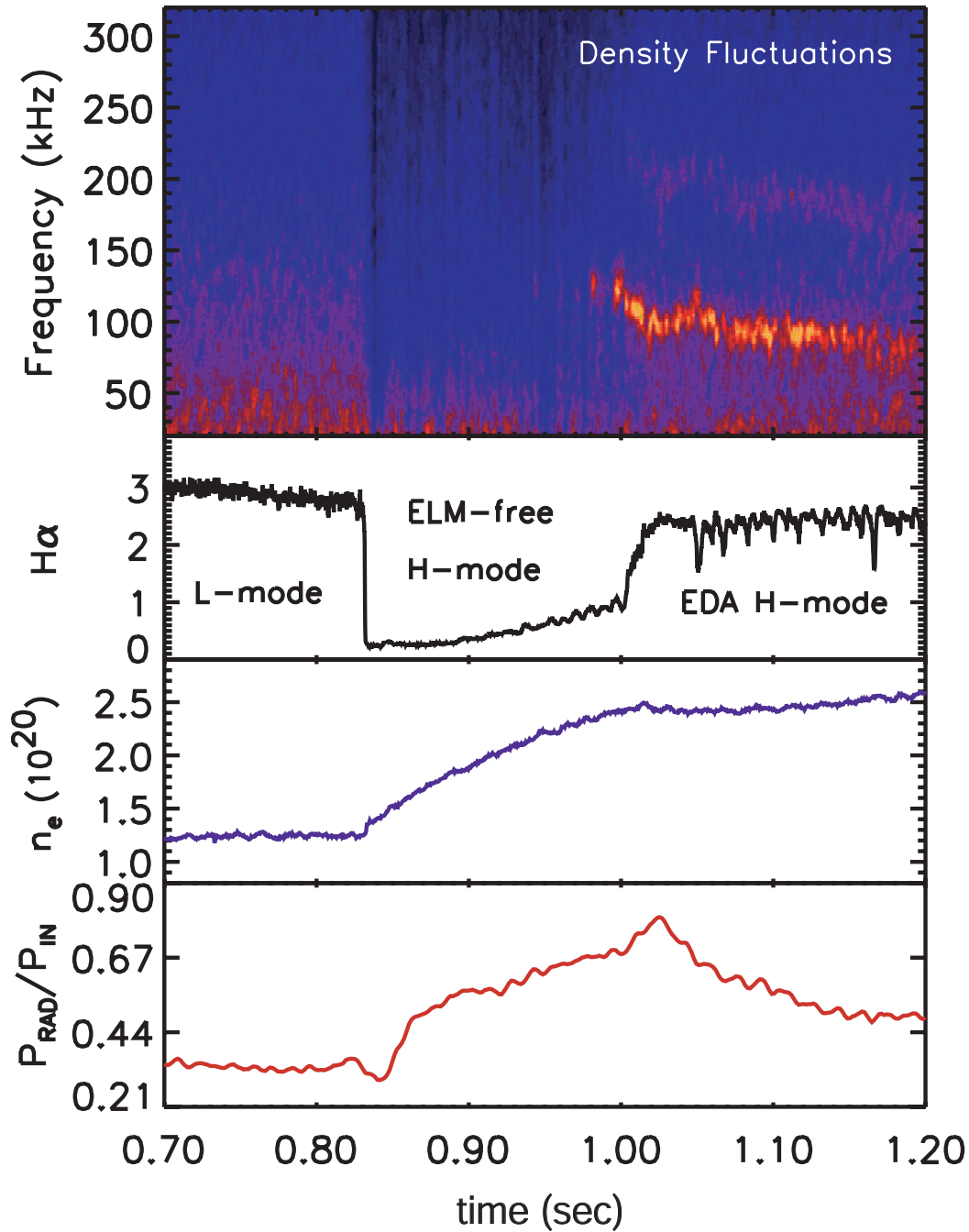


Figure 9. The EDA ELM-free boundary is plotted in q - δ space showing that EDA is more likely at higher safety factor and higher triangularity. There are significant areas of overlap suggesting that other variables are important as well.

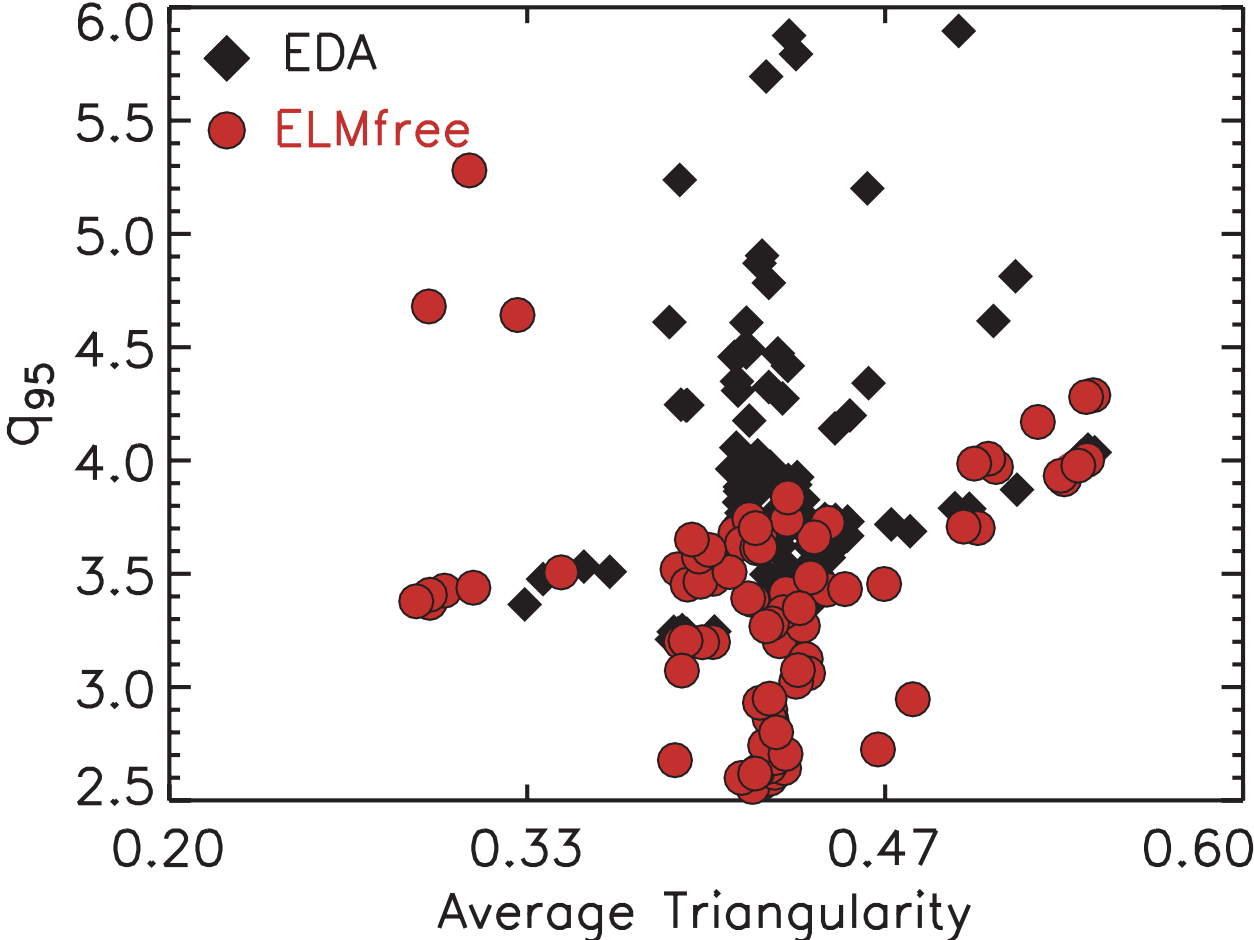


Figure 10. The boundary between EDA and small, type II ELMs is plotted in a space comprised of the edge temperature and the normalized pressure gradient (α_{MHD}). EDA tends to disappear at higher pressures and temperatures. The square symbols denote shots for which MHD stability calculations have been performed. The boundary between regimes seems to be coincident with the stability boundary for intermediate n peeling-ballooning

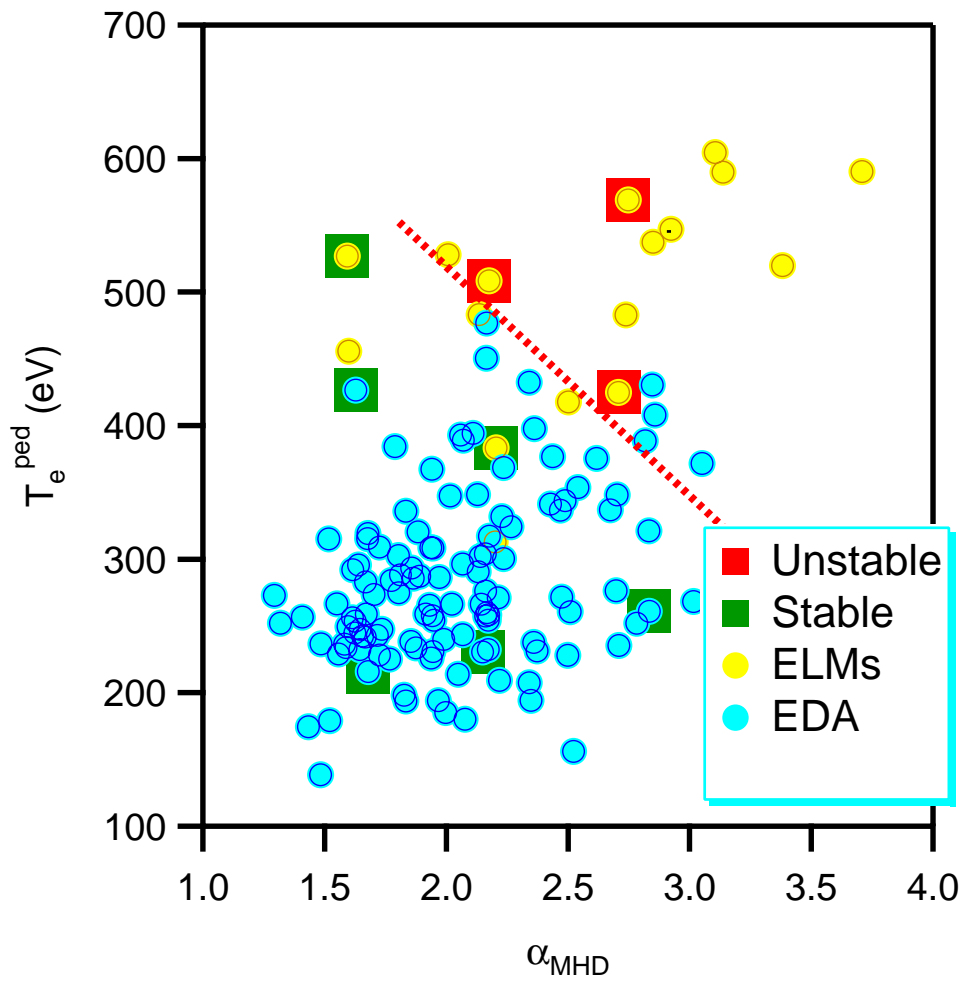


Figure 11. The effective particle diffusivity, D_{EFF} , is plotted vs the amplitude of the QC mode. The near-linear relation suggests a causal relationship between the mode and enhanced particle transport.

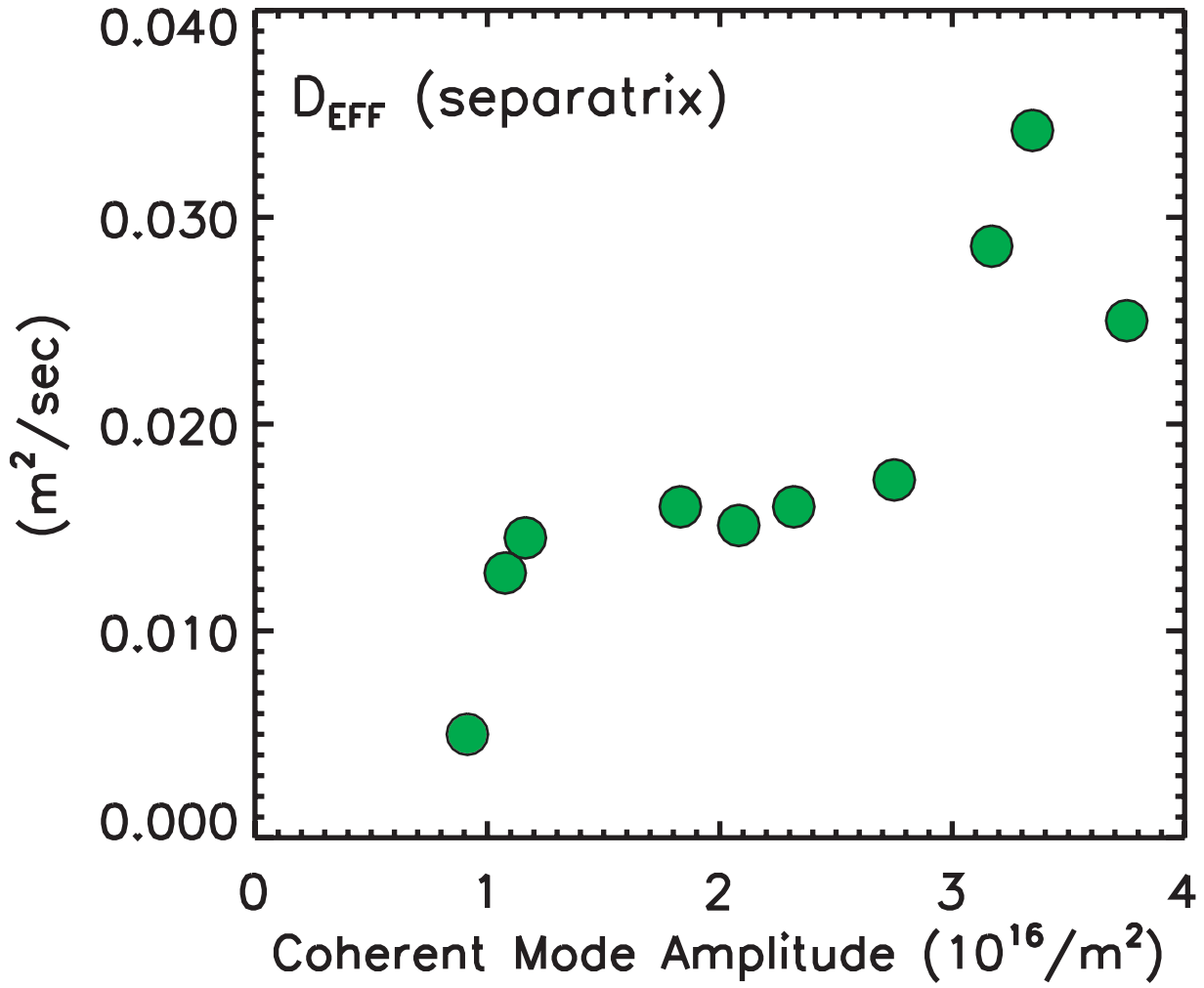


Figure 12. The QC mode autopower spectra are plotted for data from the PCI and Reflectometry diagnostics.

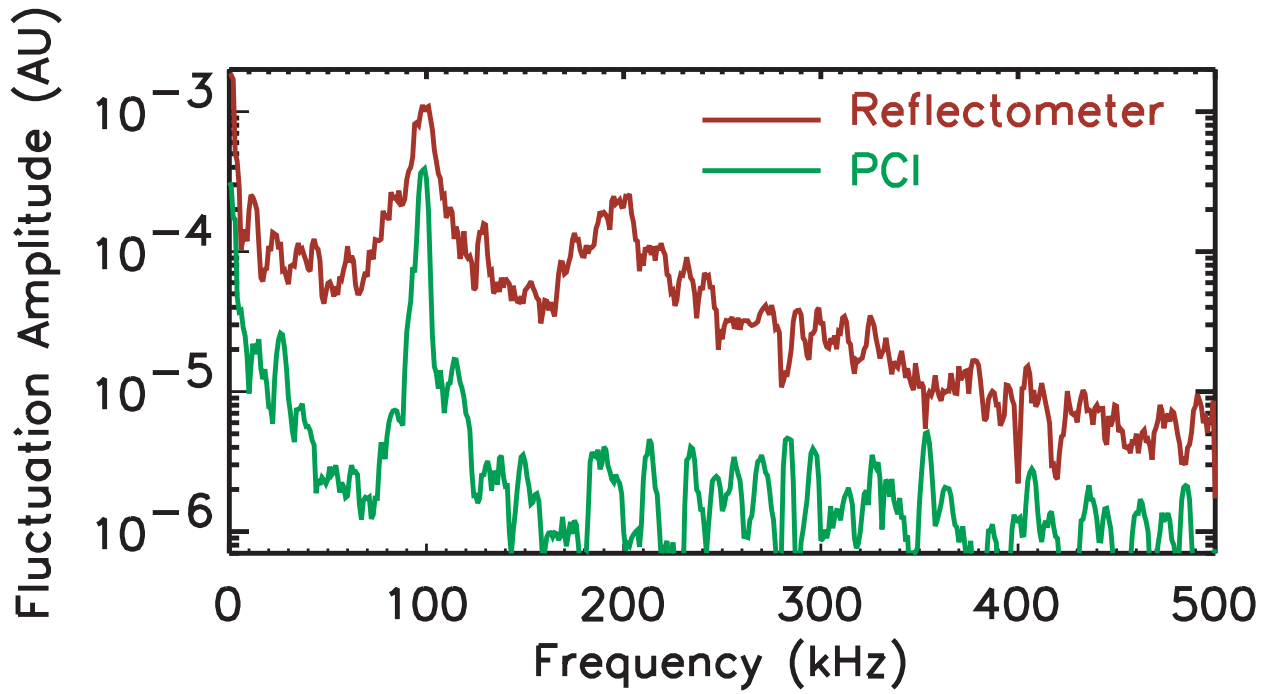


Figure 13. The evolution of the QC mode spectra showing strong downward sweeps in frequency following each transition can be seen in a discharge with three distinct H-mode periods. The change in frequency is believed to be from Doppler shifts which arise as rotation builds up in the pedestal.

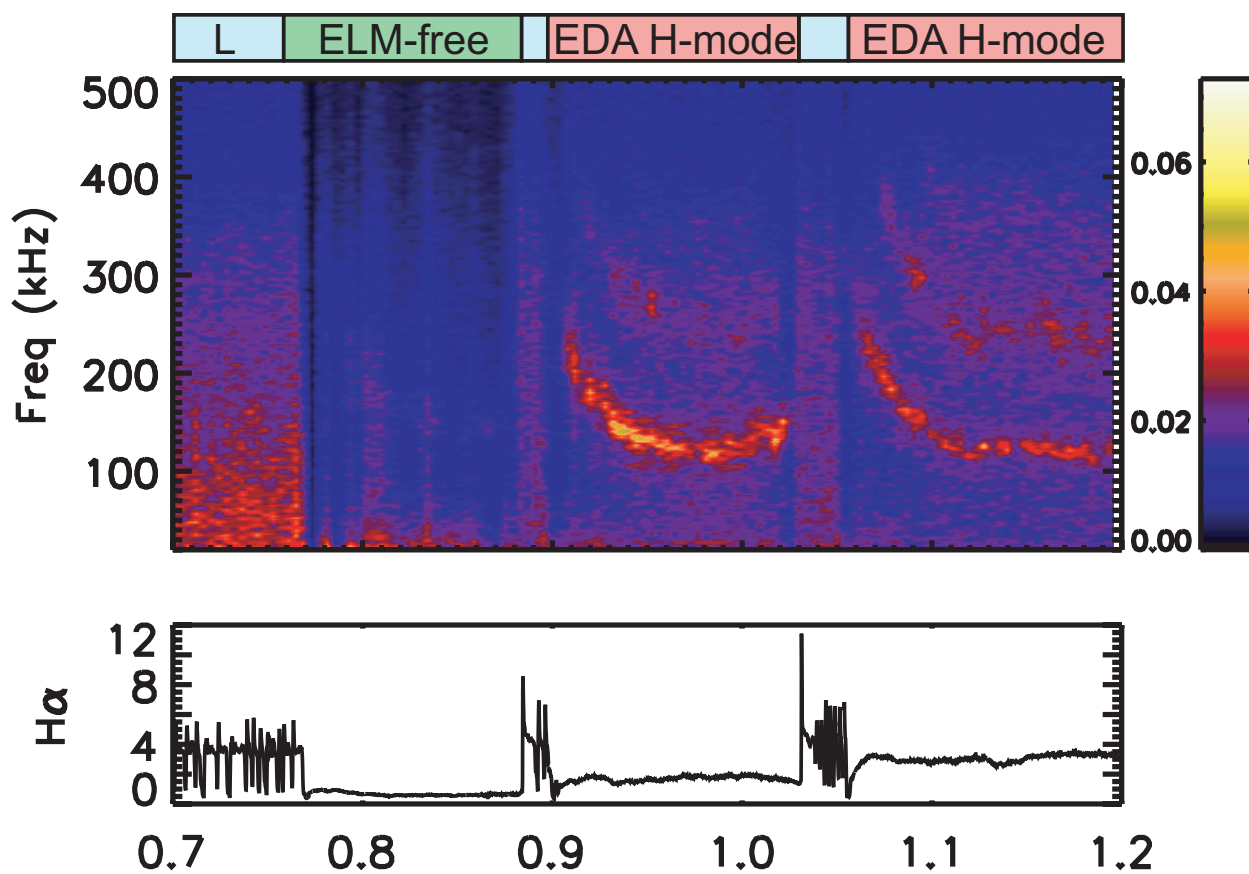
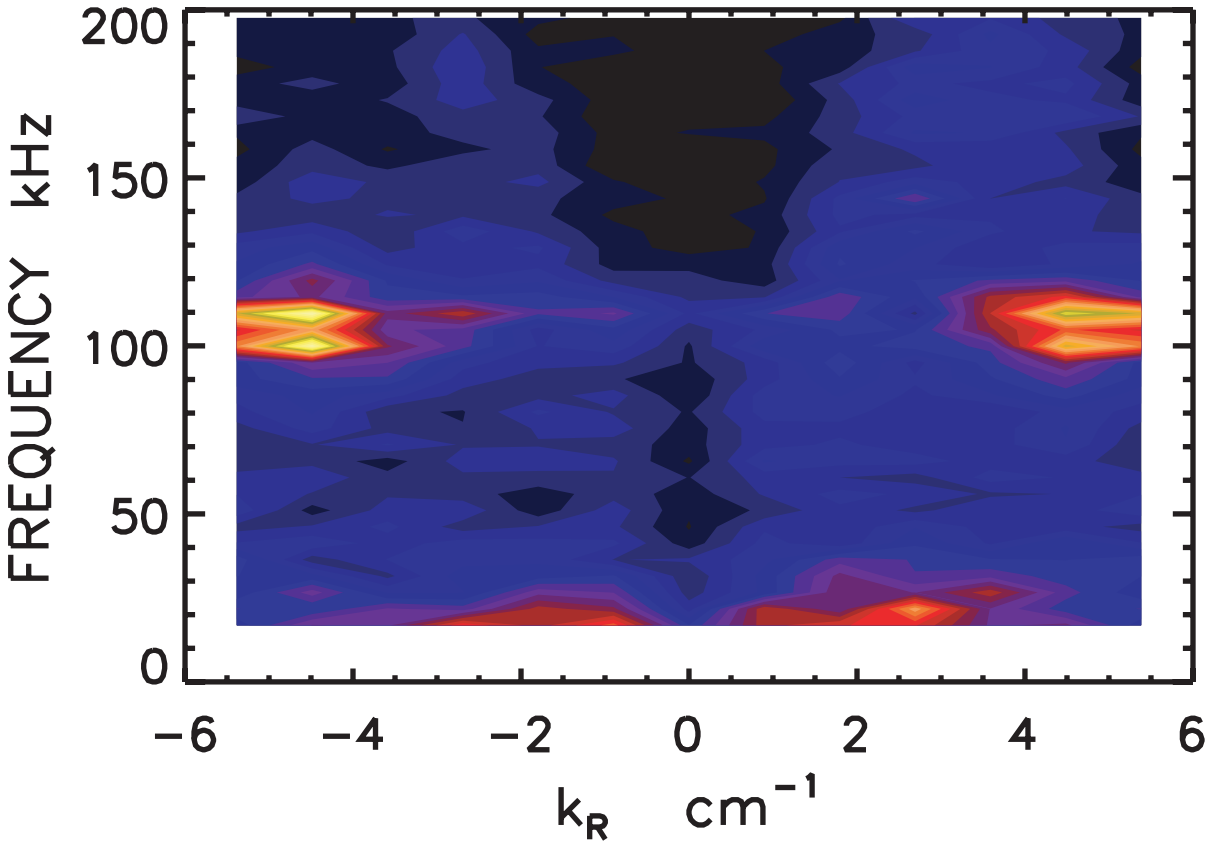


Figure 14. Wavenumber resolved spectra of the QC mode from the PCI diagnostic show well defined mode structures. The positive and negative features correspond to the top and bottom of the machine which are traversed by the PCI beam.



15. The wavenumber of the QC mode from a number of diagnostics, compared to the predictions for a field aligned perturbation, show good agreement.

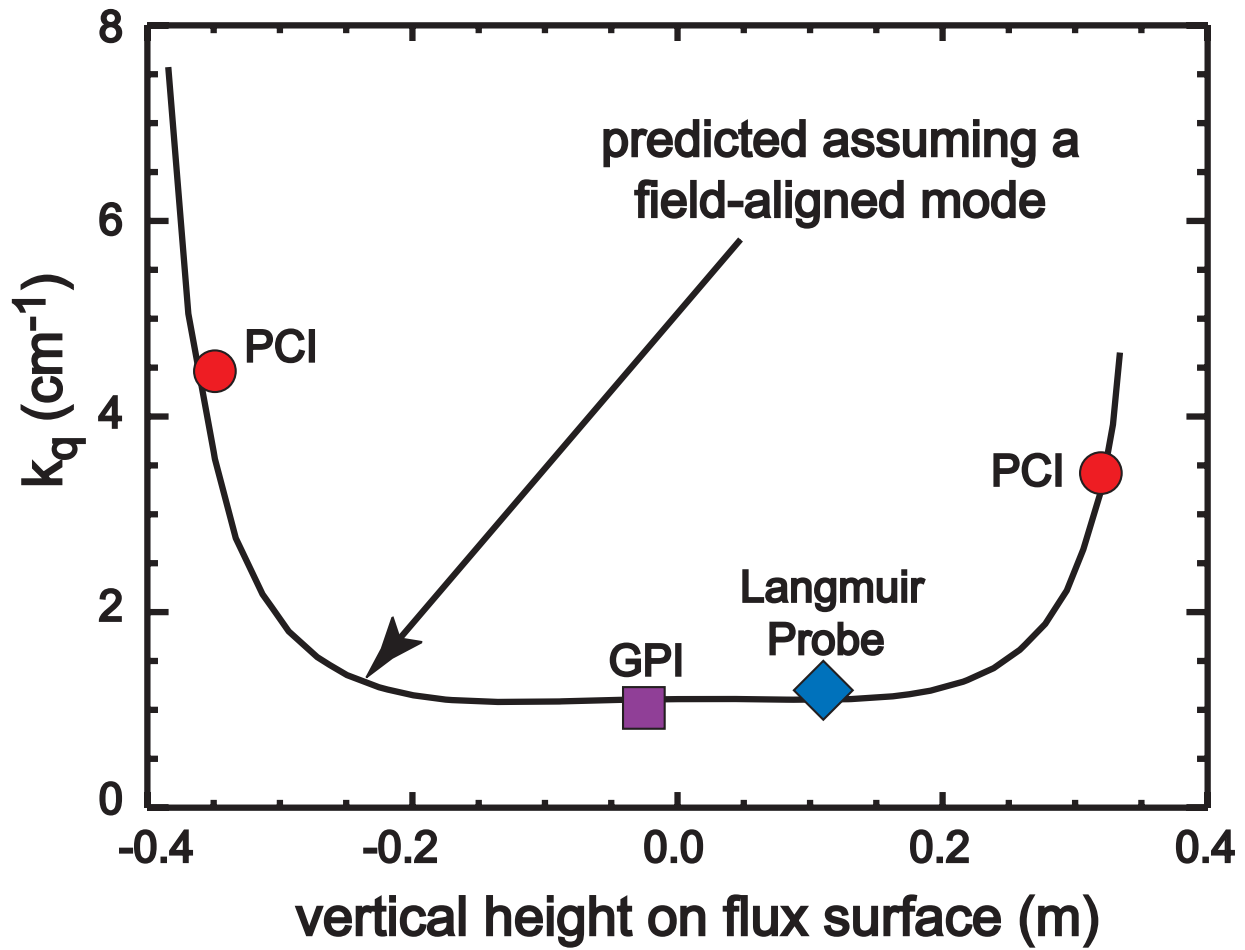


Figure 16. The QC mode amplitude, taken from scanning probe data, is plotted vs radius. From this measurement, a mode width of 1-2mm is inferred. The shaded region represents the separatrix with uncertainty from the equilibrium mapping.

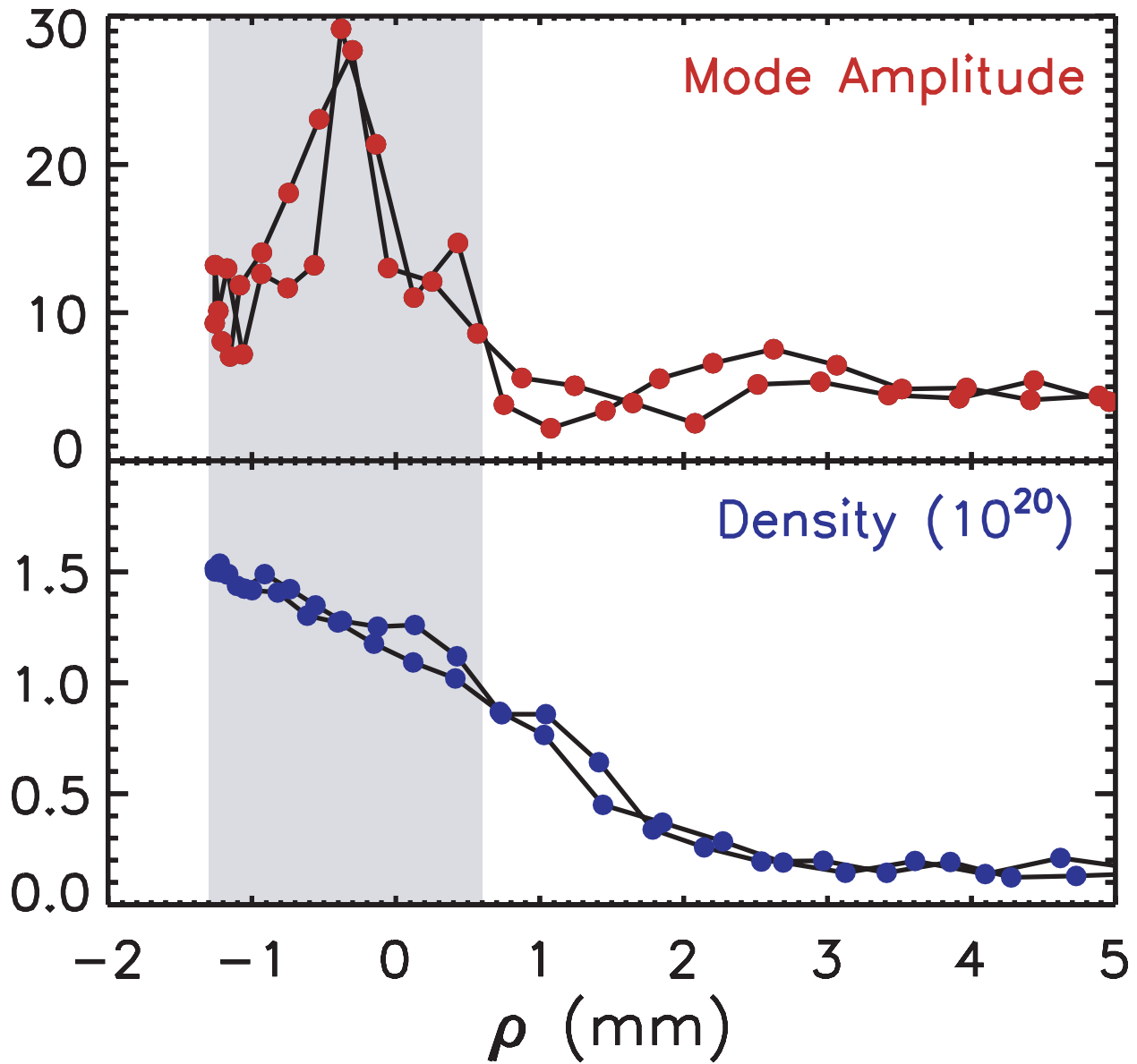


Figure 17a. H-mode confinement data from C-Mod are significantly above the predictions of the ITER93 ELM-free scaling law, which was derived prior to C-Mod operation.

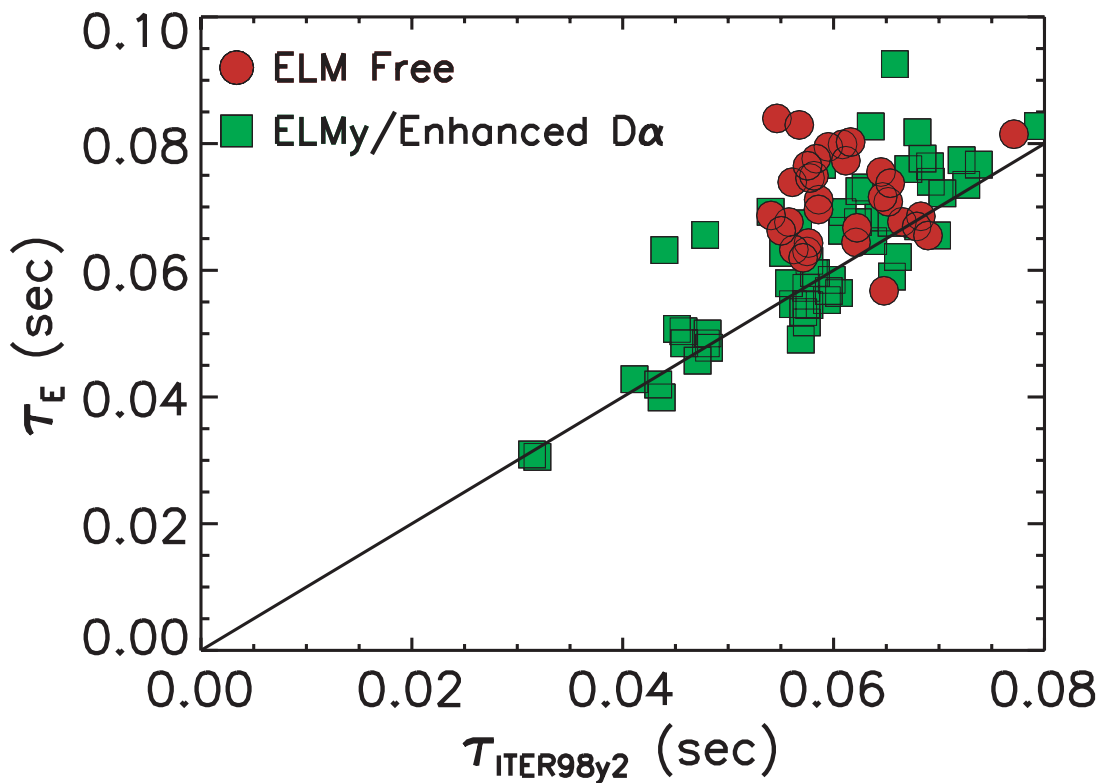
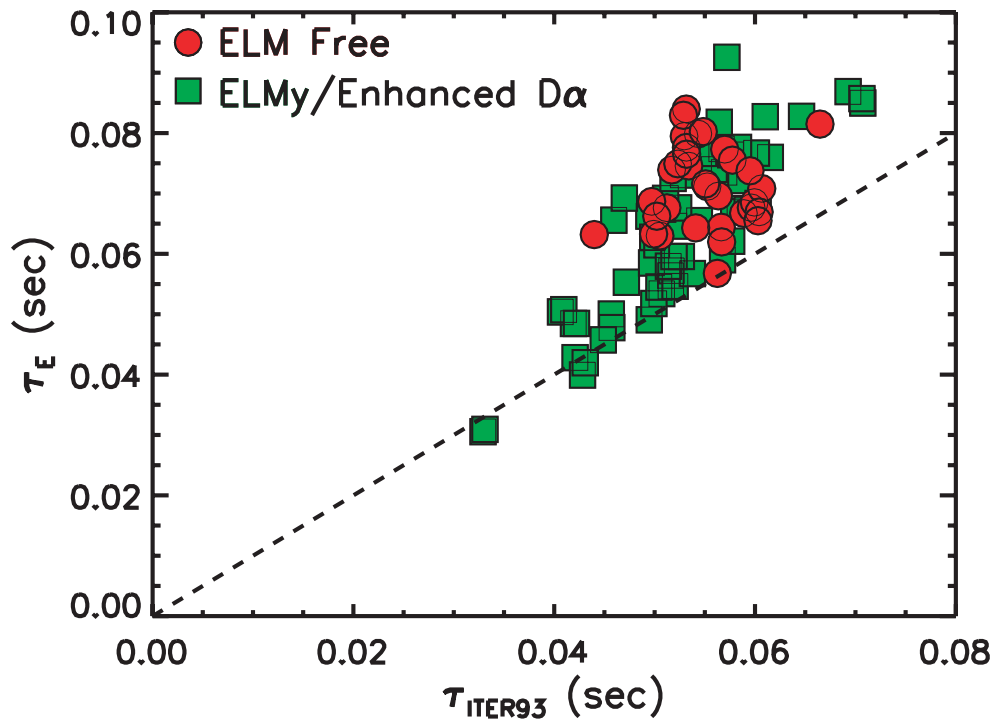


Figure 17b. After C-Mod data were added to the international database and the regressions recalculated, the agreement improved.

Figure 18. The confinement enhancement factor H_{ITER89} is plotted against $f_{RAD} \equiv P_{RAD}/P_{TOTAL}$ for both L and H-mode discharges. The L-mode confinement is seen to be insensitive to this parameter while confinement in the H-mode plasmas drops when f_{RAD} rises above 0.5.

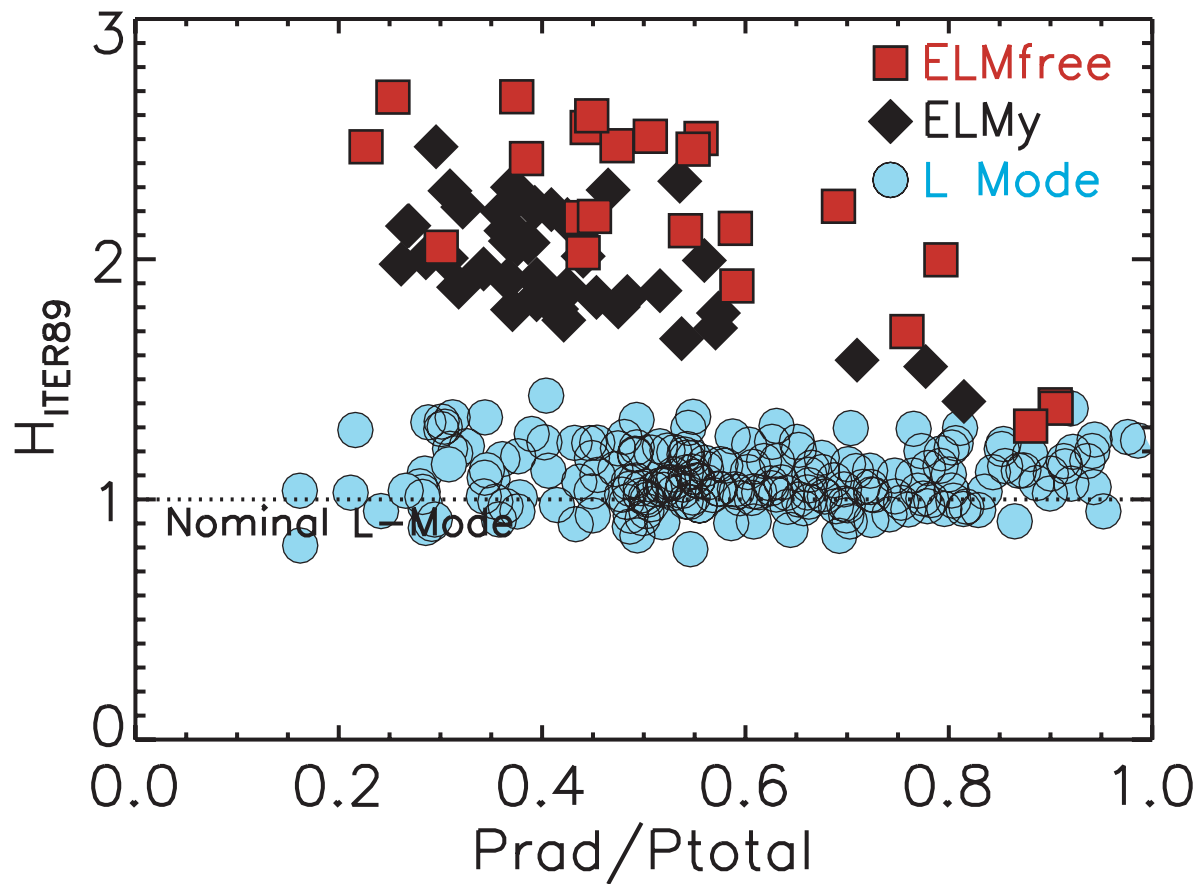


Figure 19. Profiles of radiated power taken before and after boronization, indicate a dramatic drop in high-Z impurity content following the wall treatment.

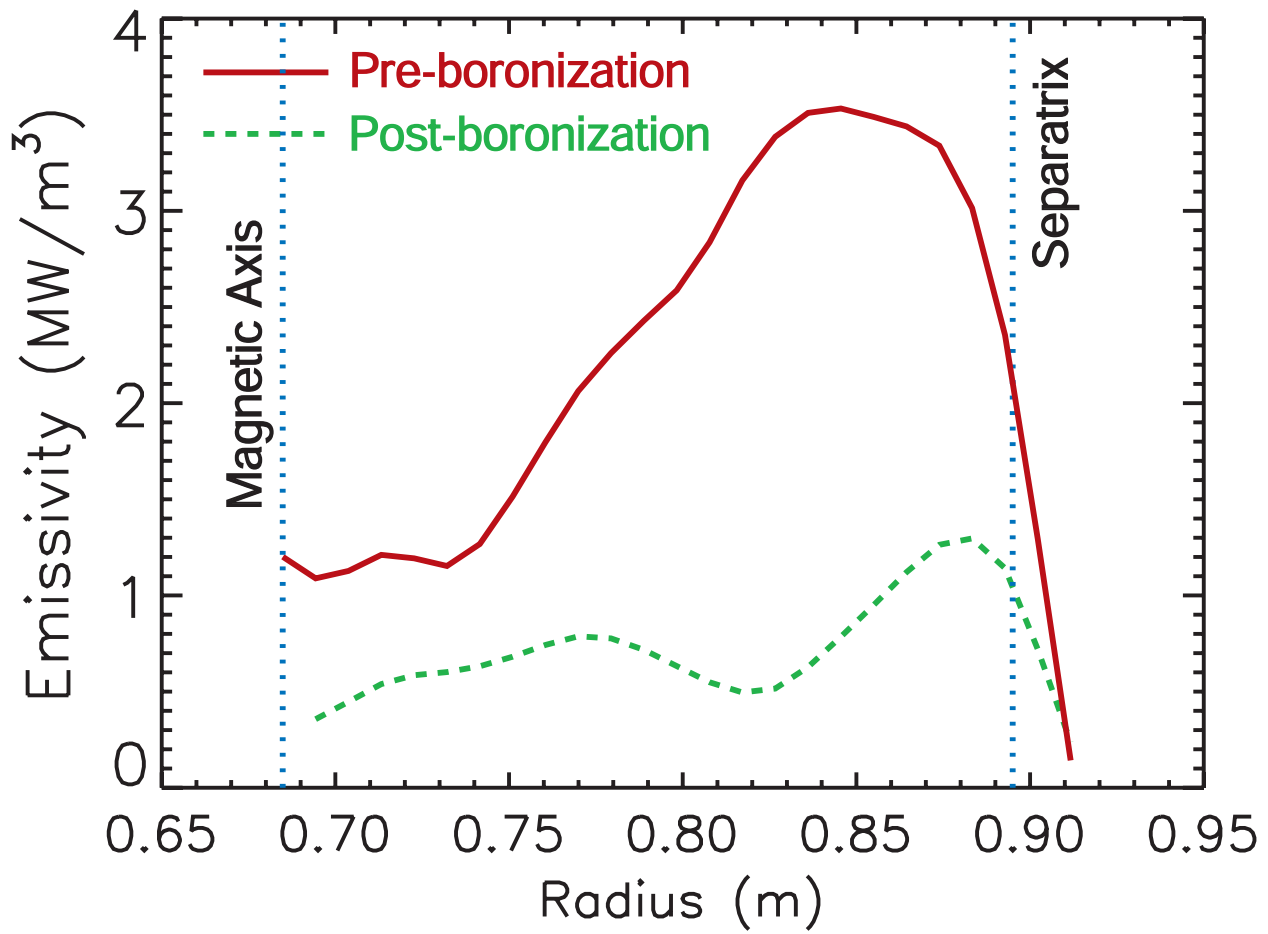


Figure 20. The H factor is plotted vs outer gap, showing that confinement does not deteriorate if the plasma wall spacing is larger than 2-3 mm. This distance roughly corresponds to the scrape-off layer width. H-modes were not obtained in discharges limited on the outer wall.

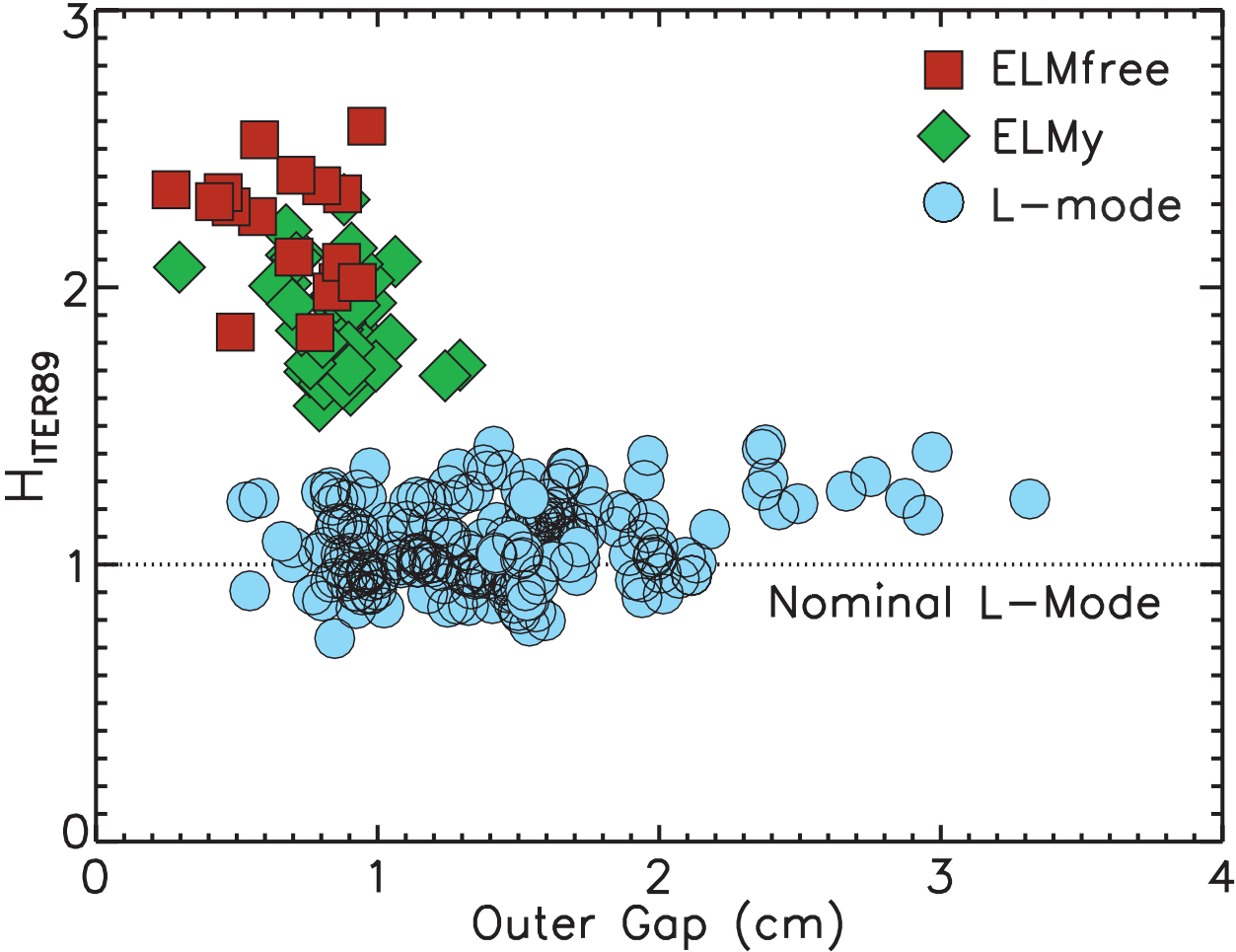


Figure 21. The H factor is plotted vs $P/P_{THRESHOLD}$. Good confinement is achieved if the heating power is at the threshold computed for the fully developed H-mode. It is important to note that this level of input power is two to four times the threshold power as computed for the target plasma.

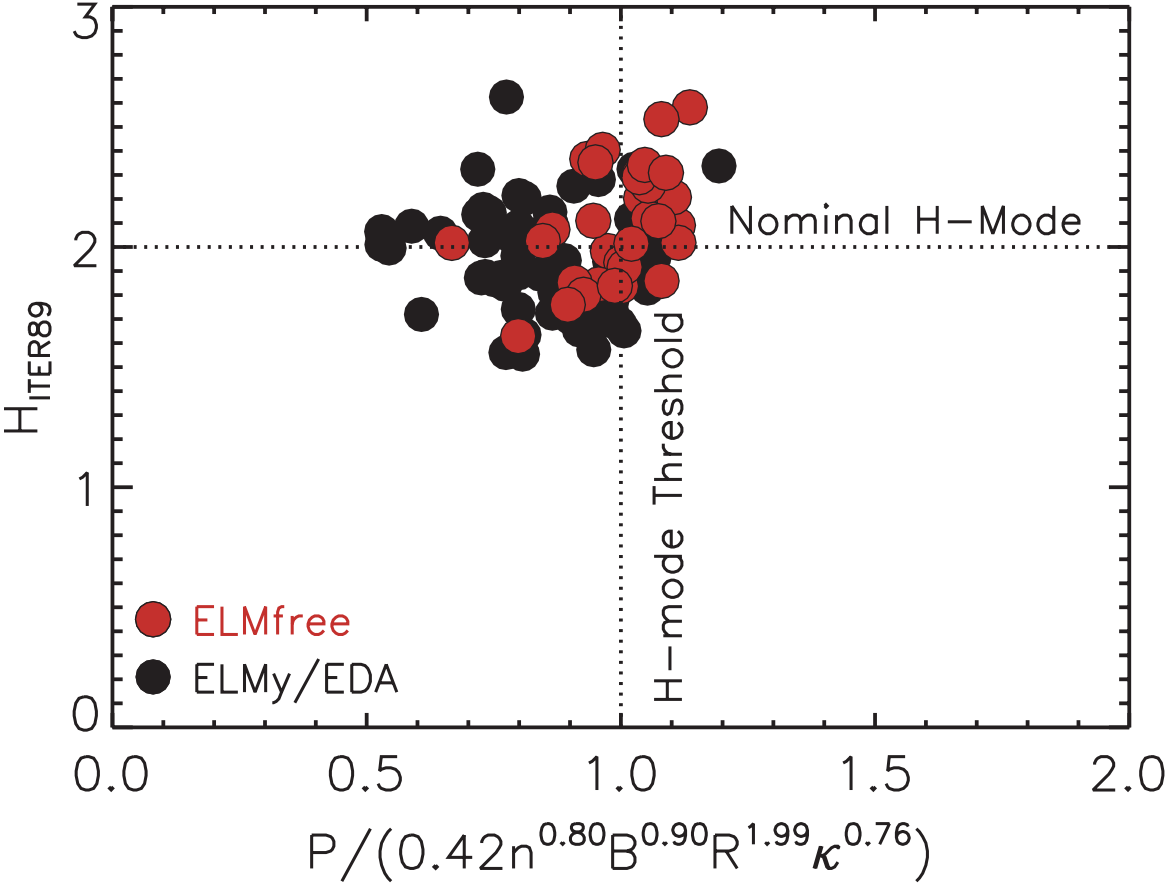
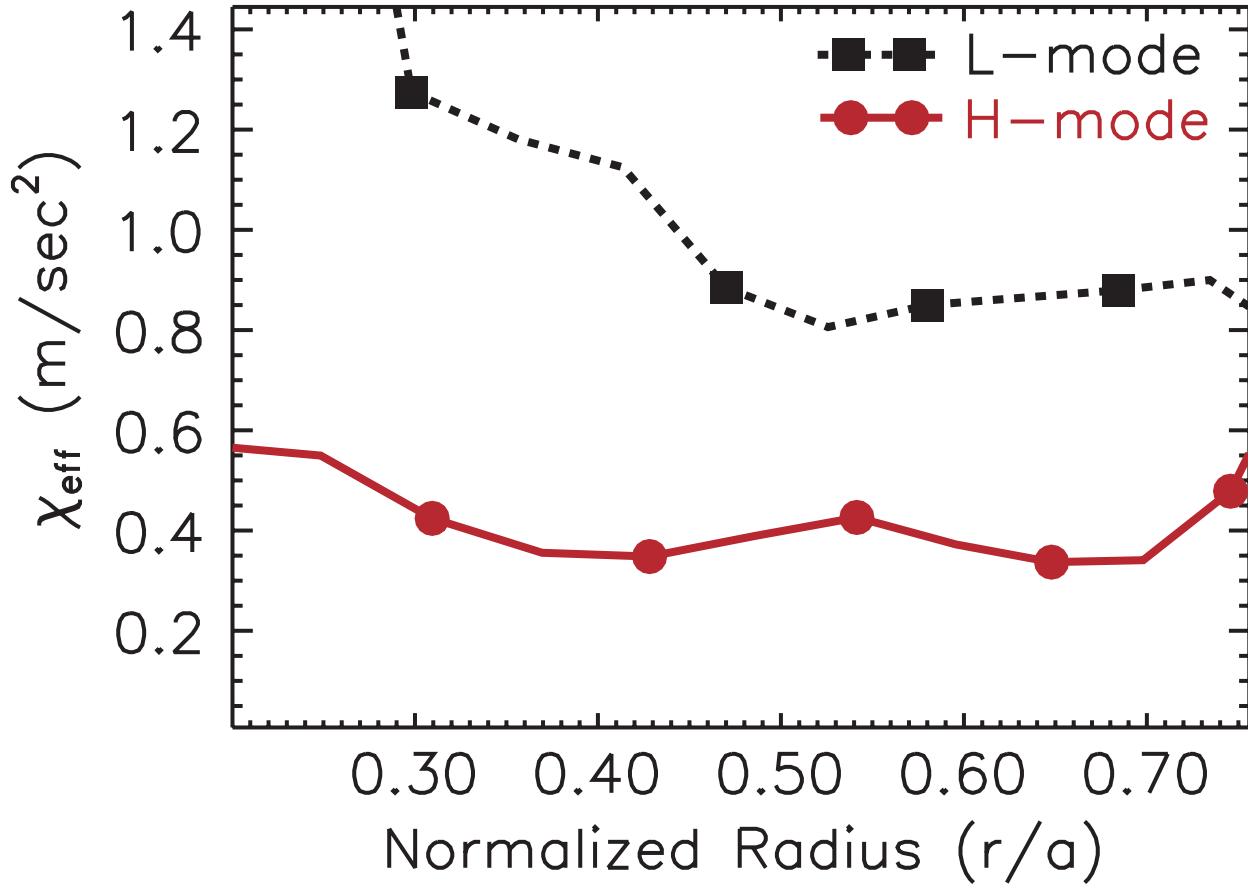


Figure 22. The effective thermal diffusivity, χ_{EFF} , is compared between a matched L-mode and H-mode pair of discharges. The L-mode discharge was taken with reversed field to suppress the transition, despite the strong heating.



23. Particle transport coefficients, calculated from the plasma response to a set of gas puffs, are plotted vs radius. Note that thermal and particle diffusivity are similar in value.

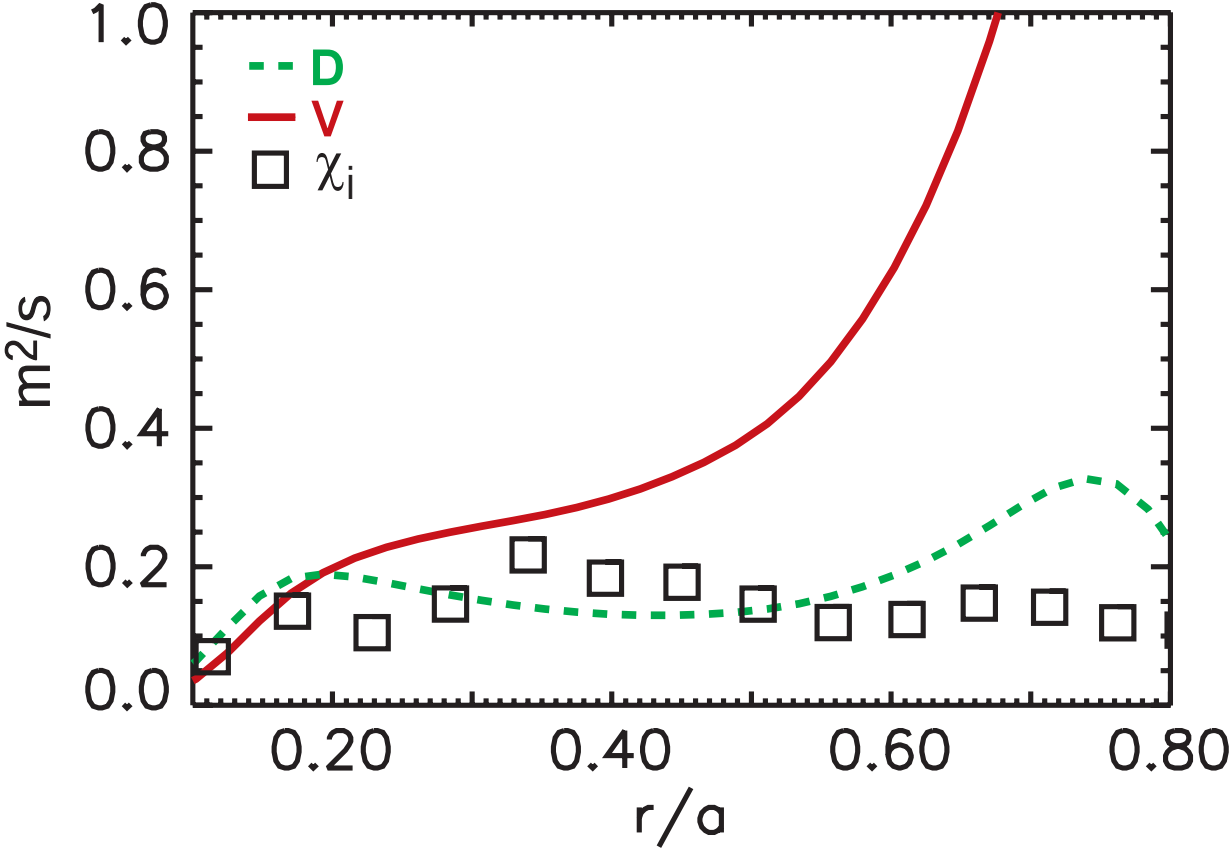


Figure 24. Measured T_e profiles were found to be significantly above those predicted by several physics-based models. The discrepancy was apparently resolved by nonlinear turbulence calculations. (The upturn in the predicted T_e profiles near the magnetic axis can be attributed to the lack of sawteeth in the models.)

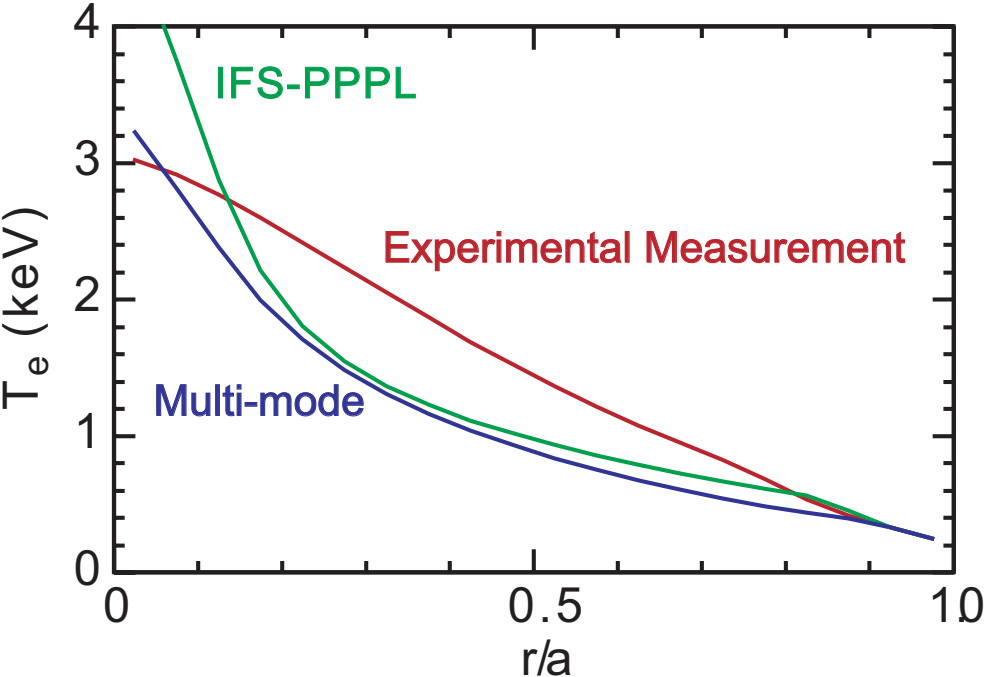
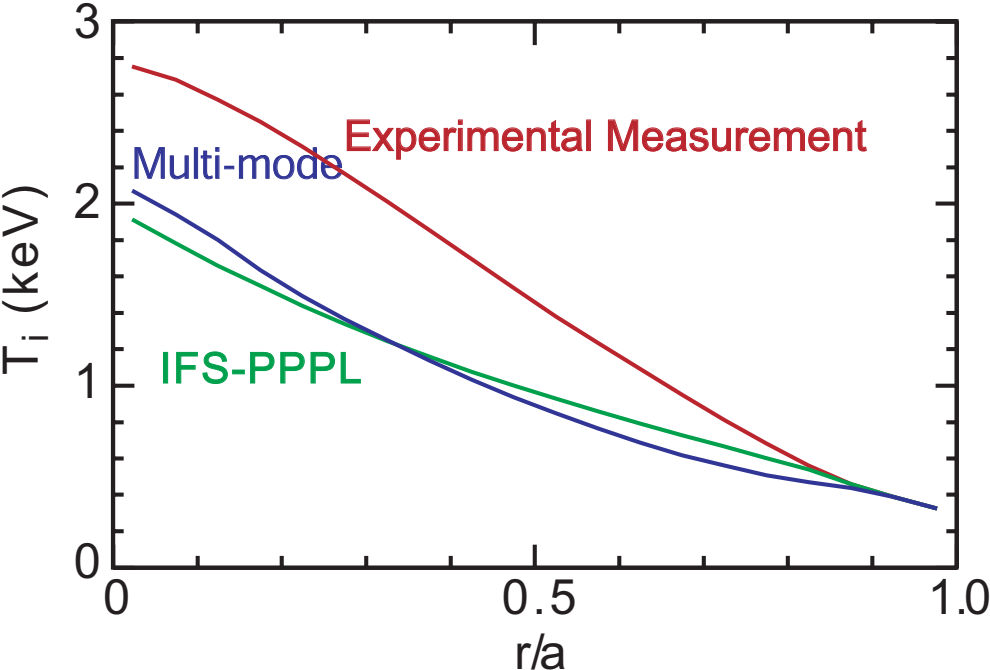


Figure 25. The confinement enhancement factor, H is seen to be tightly correlated with the pedestal temperature across confinement regimes

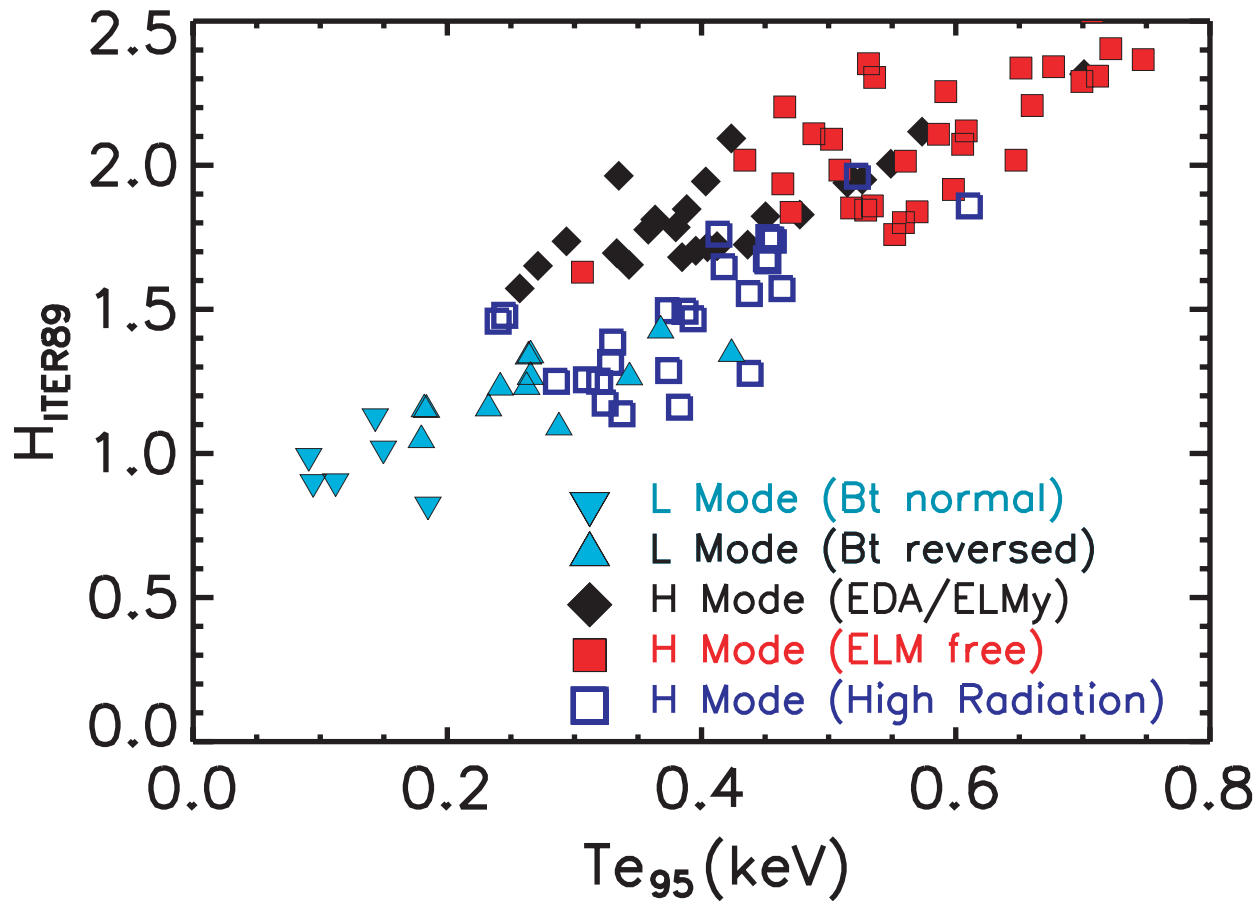


Figure 26. Temperature profile self-similarity (with the local gradient proportional to the local value) is demonstrated here in a semi-log plot of profiles using data from 100 shots chosen randomly from the 2003 and 2004 experimental campaigns. The data were restricted to steady, sawtoothed discharges at 1MA and 5.3T, to hold the magnetic shear approximately constant. For consistency, data is plotted at the top of each sawtooth nearest the random time chosen. Otherwise the data contains all powers, plasma densities and is a mixture of L and H-modes.

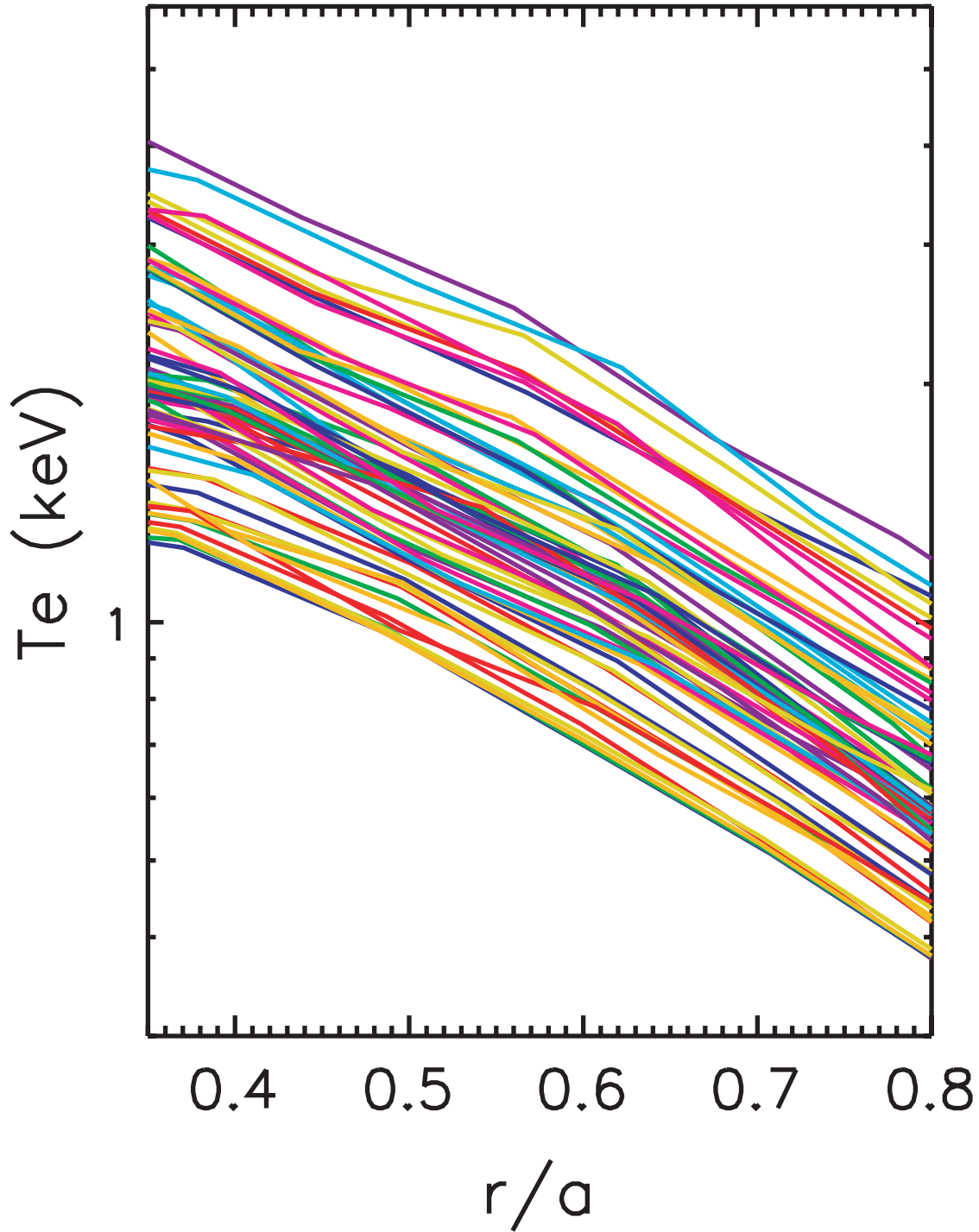


Figure 27. The core temperature gradient is also seen to be tightly correlated with pedestal temperature, accounting for the increase in stored energy and confinement.

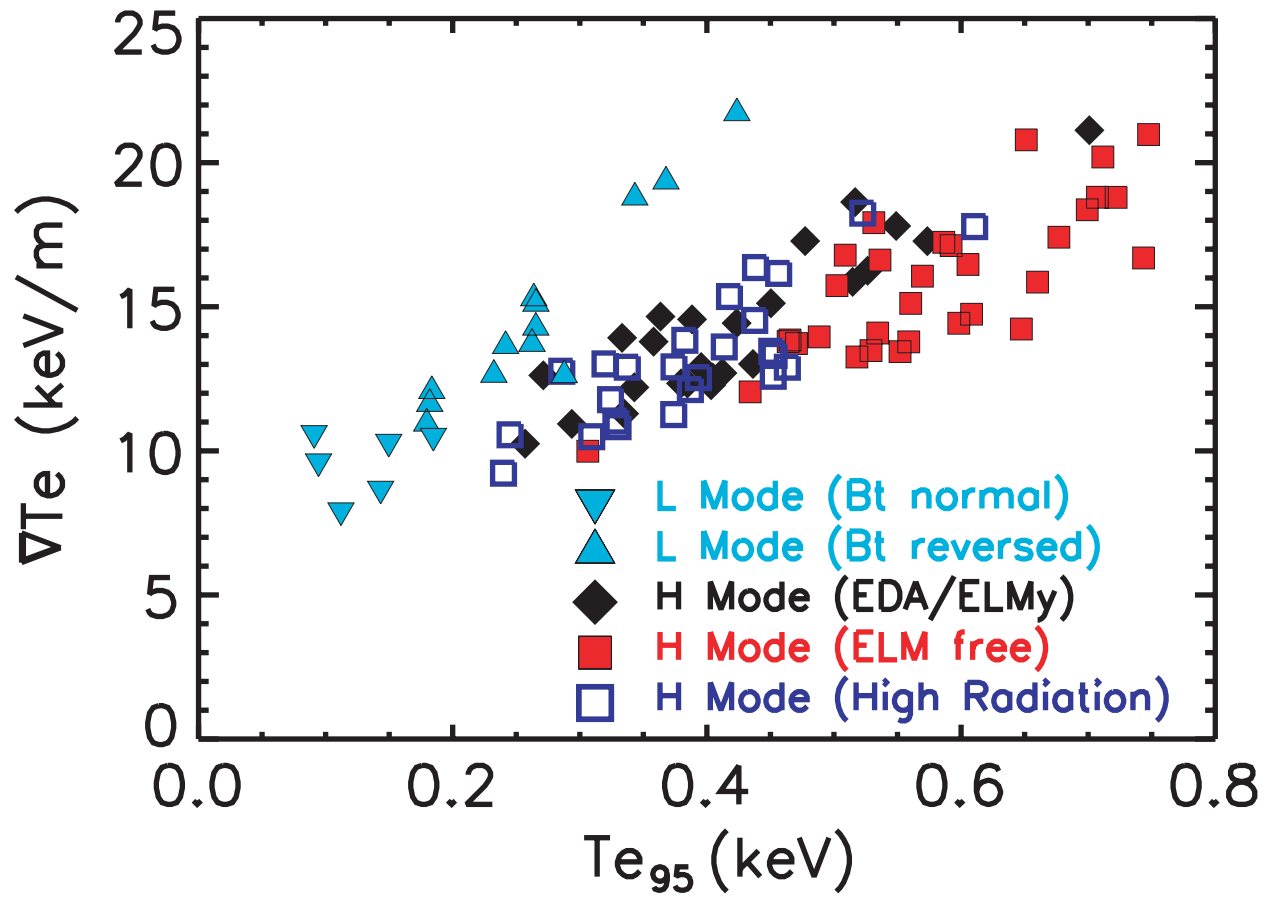


Figure 28. The pedestal temperature is plotted vs power per particle. Following the results seen in figures z, aa and bb, the principal difference between core transport in L-mode and H-mode is the ease with which high edge temperatures are obtained in the latter regime.

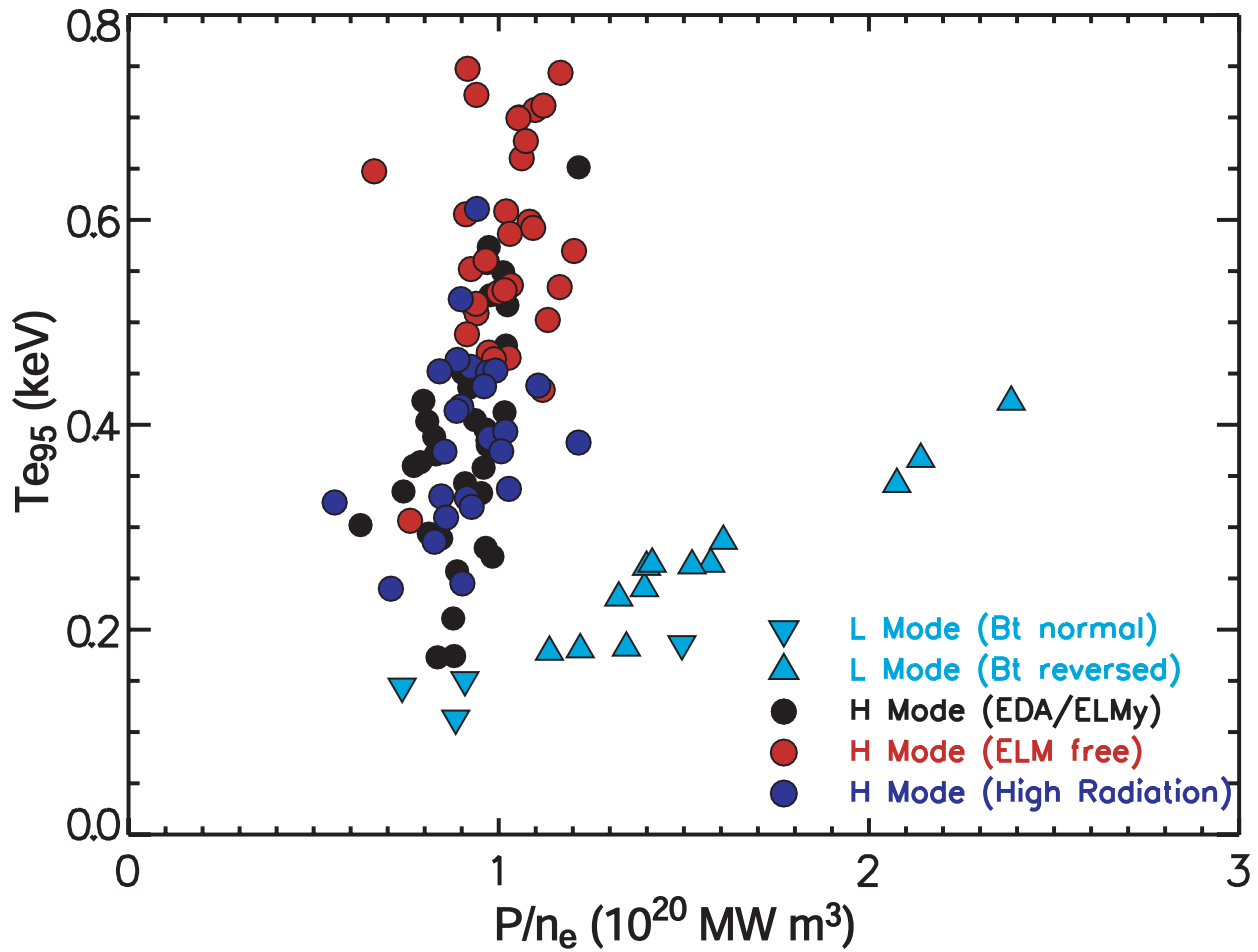


Figure 29. A direct demonstration of the tight connection between edge and core temperatures was obtained in experiments in which radiating gases were puffed into developed H-modes. Radiation was peaked at $r/a \sim 0.8$, and resulted in a strong cooling of the pedestal. A corresponding decrease in core ∇T was observed, despite the fact that 90% of the radiated power was outside this radius. As in the global dataset, the temperature scale length L_T remained constant

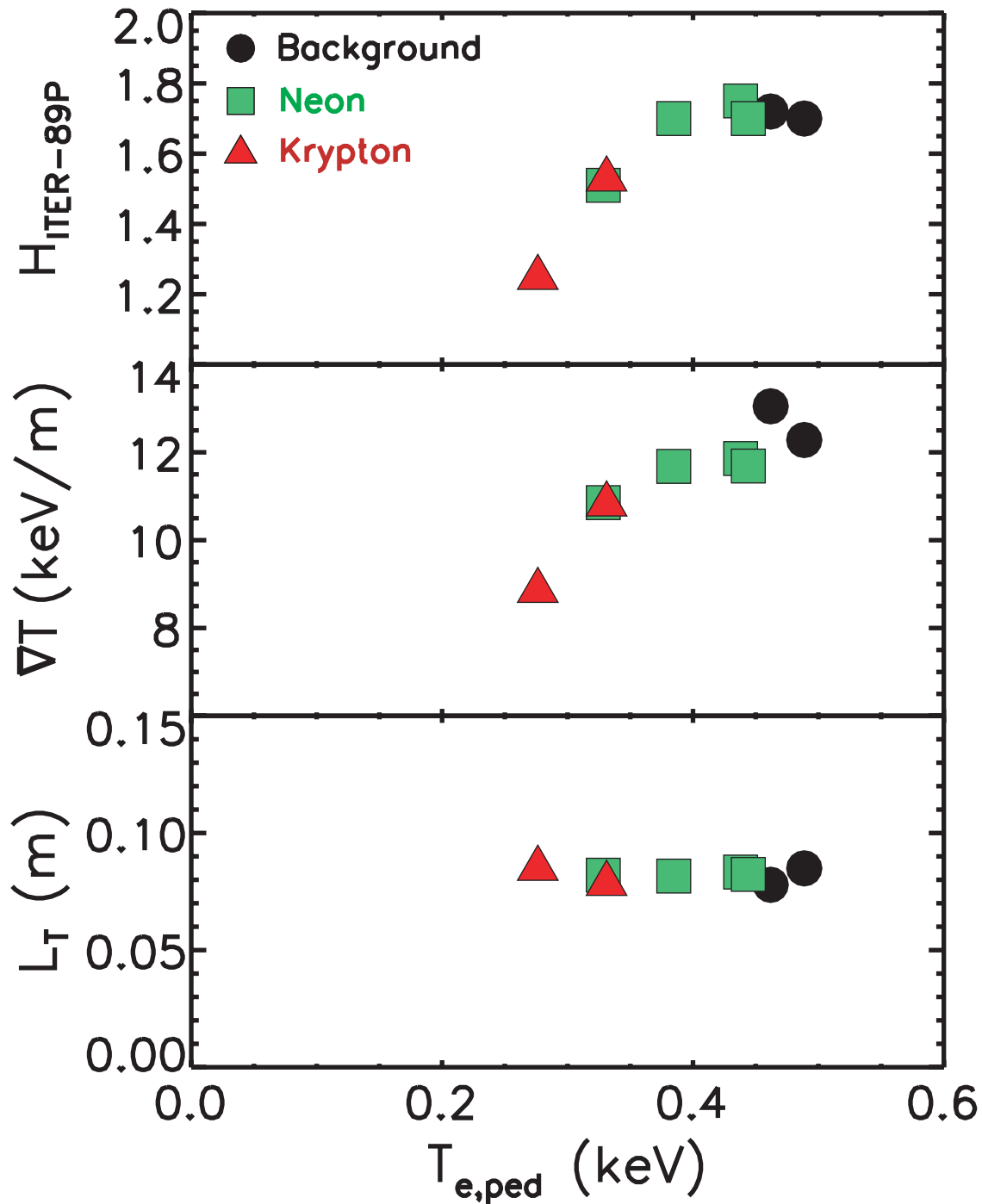


Figure 30. The normalized temperature gradient, R/L_T is plotted vs input power. The constancy of the gradient is consistent with marginal stability and the predictions of the critical gradient for ITG modes from theory.

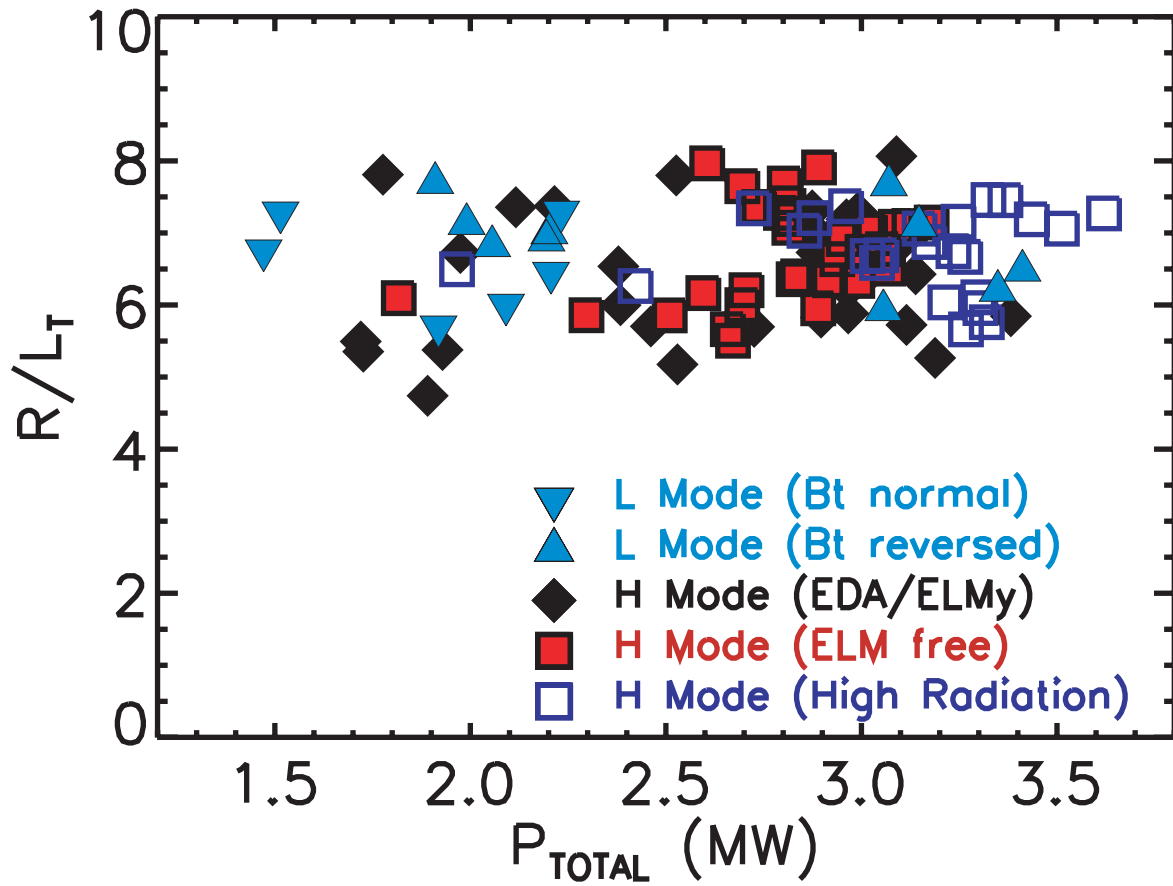


Figure 31. Results of a detailed calculation of the critical gradient are shown. The experimental heat flux and gradient are consistent with the nonlinear computation. The upshift in critical gradient in the calculation is due to stabilization of ITG turbulence by zonal flows. This result helps to explain the discrepancy seen in figure v.

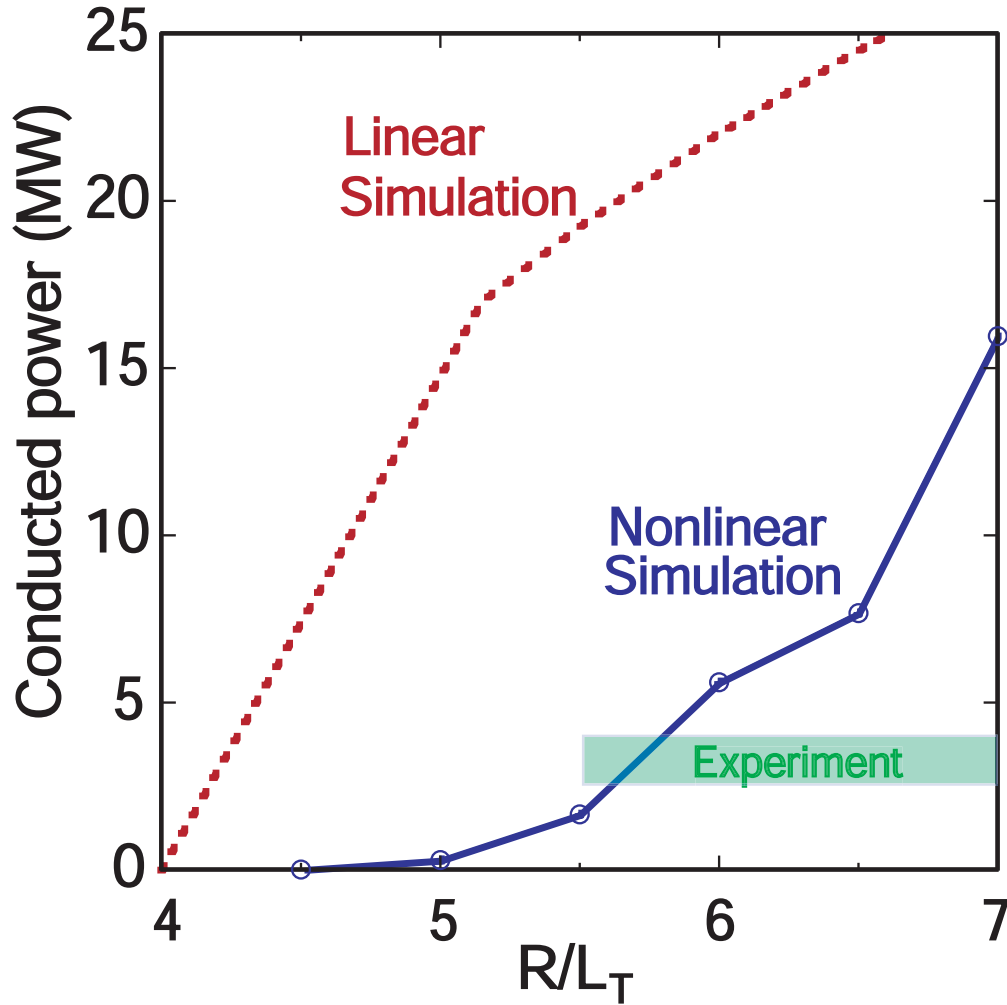


Figure 32. The brightness of niobium impurity lines following injection into two different discharges. After a brief influx phase, the impurity accumulated in an ELM-free discharge, but not in the EDA discharge. The ELM-free H-mode was transient and following its return to L-mode at 0.973 sec, the rapid loss of the impurity was apparent.

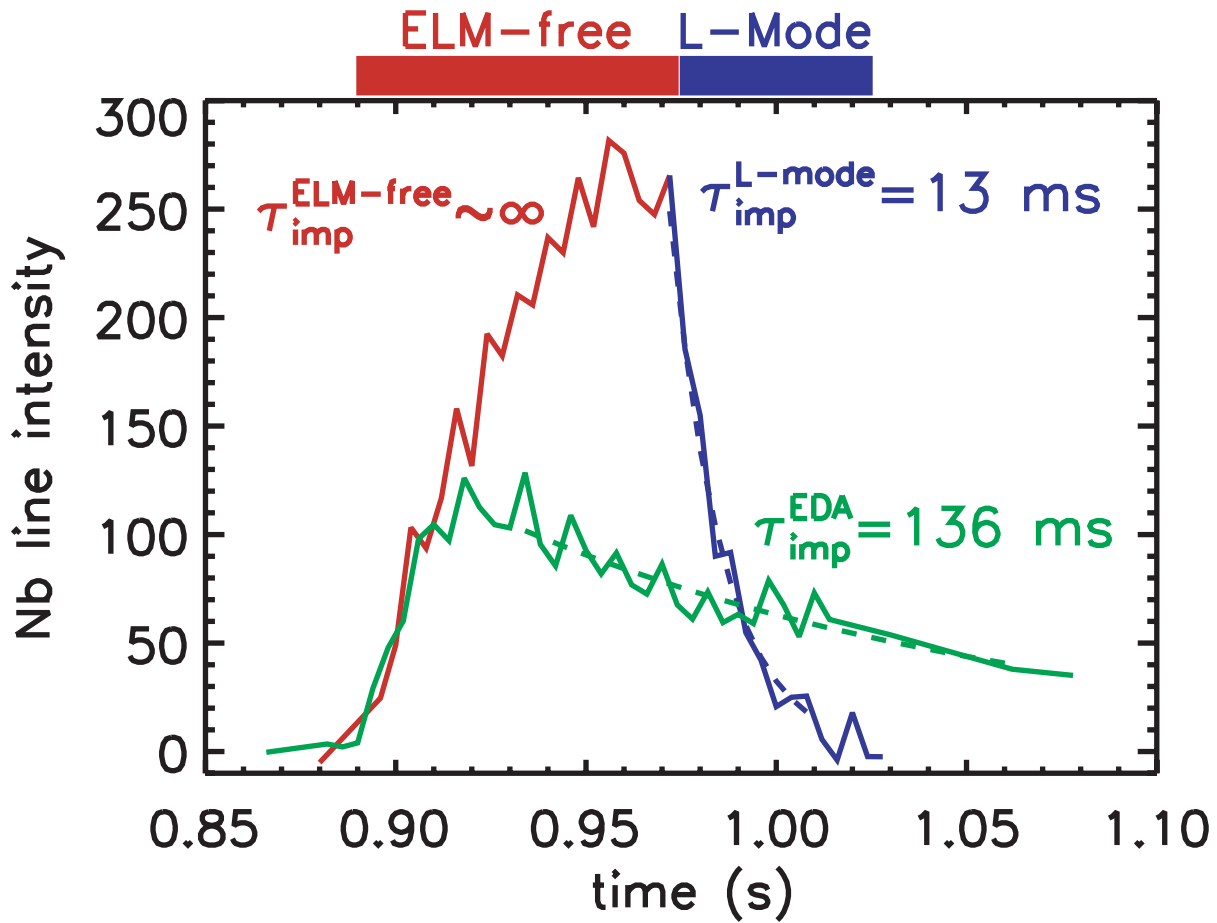


Figure 33. The difference in impurity confinement between the H-mode regimes is clear in this discharge where scandium was injected into a developed ELM-free plasma which later made a spontaneous transition to EDA at 0.86 sec. The long impurity confinement time in the ELM-free phase contrasts with the decreased particle confinement in the EDA phase which followed.

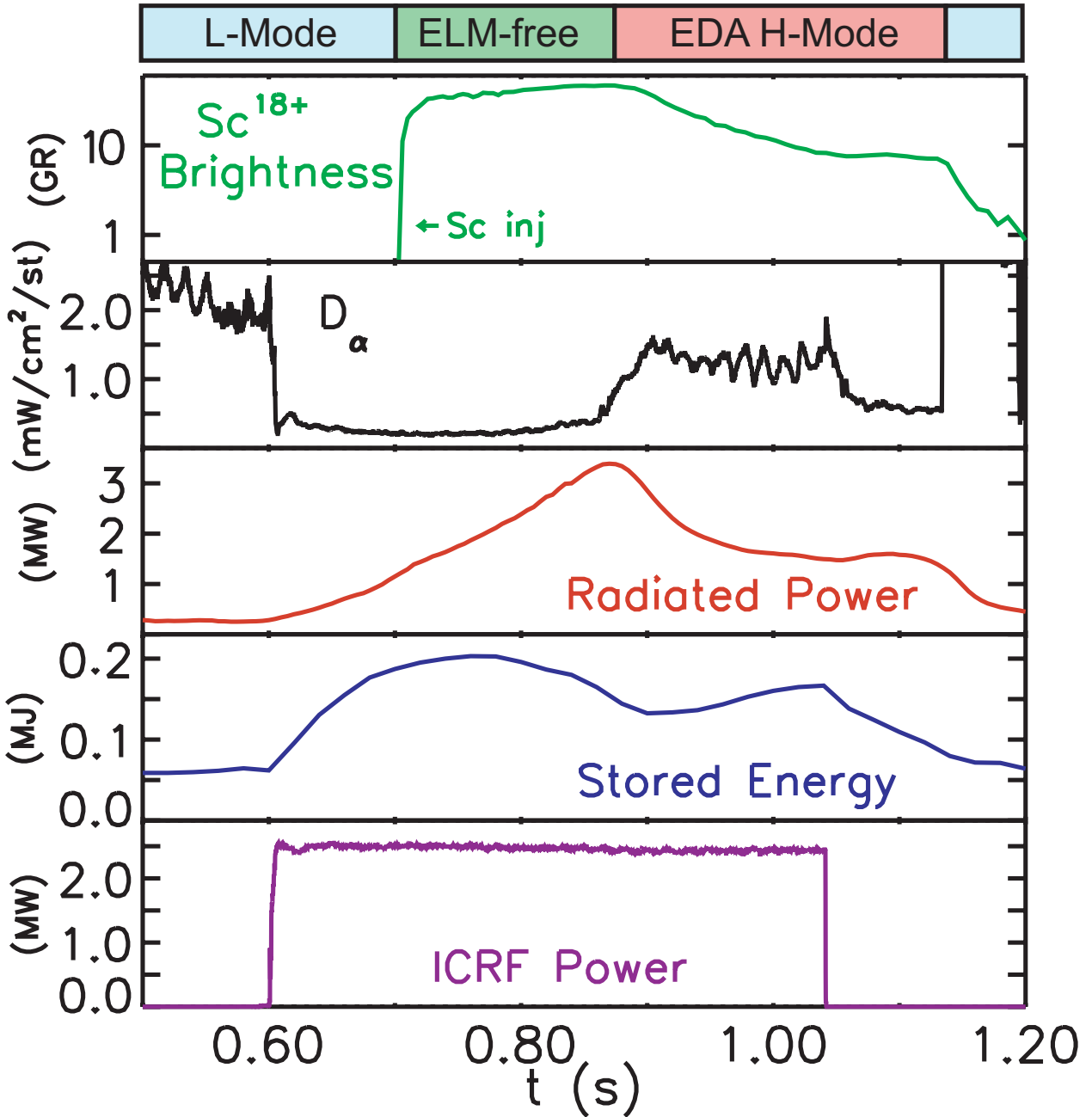


Figure 34. Appropriately scaled plasma profiles are shown for two discharges in a dimensionless identity comparison of C-Mod and DIII-D. Reasonable matches were obtained across the profiles. The largest difference was the somewhat more peaked power deposition obtained with ICRF heating on C-Mode compared to the NBI heating on DIII-D. Since it is the integrated power flux which enters the transport calculations, this difference is not believed to be important over most of the plasma.

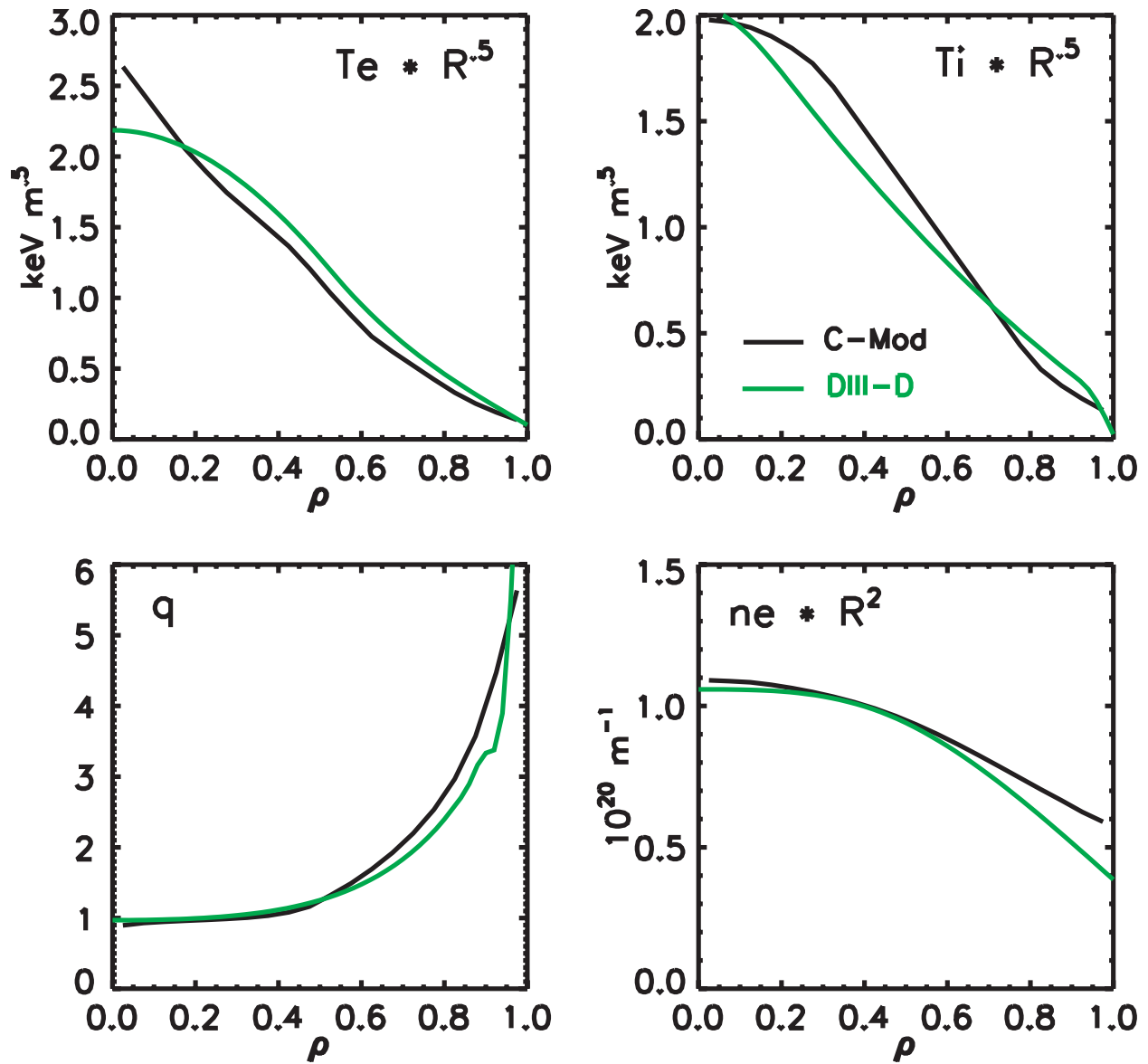


Figure 35. A pair of dimensionless pedestal comparisons, from C-Mod and DIII-D, show that the entire profile could be matched, suggesting a primary role for plasma physics in determining the edge profiles

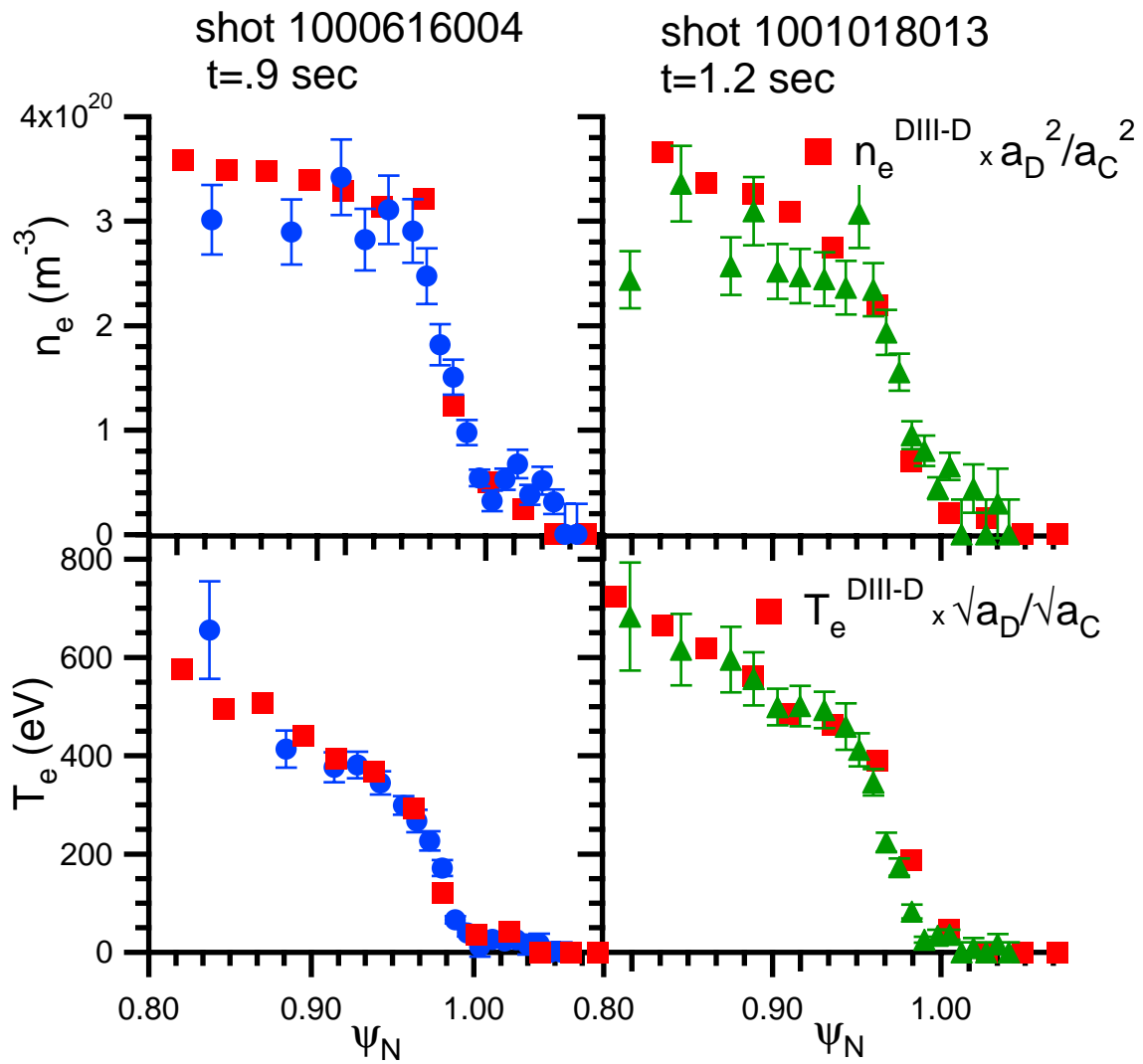


Figure 36. An example of dimensionless scaling, in which the normalized confinement time is plotted against collisionality with all other dimensionless parameters (β , ρ^* , ε , δ , κ , etc) held constant. The decrease in confinement at higher collisionality is consistent with predictions from theories of collisional damping of zonal flows.

